Final Report of the Project "Efficient Safety and Degradation Modeling of Automotive Lithium-ion Cells and Packs"

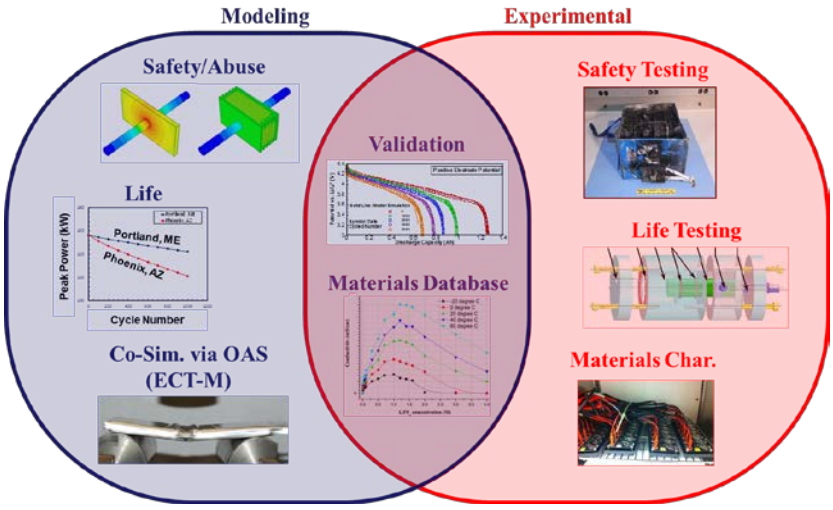

A Final Report Submitted to
Department of Energy and National Energy Technology Laboratory
Under Award No. DE-EE0006425

Principal Investigator: Chao-Yang Wang
Prepared by EC Power CAEBAT2 Project Team
In Collaboration with Penn State University Subcontract Team

EC Power
341 Science Park Road
State College, PA 16803
Ph: 814-861-6233
Fax: 814-861-6234
http://www.ecpowergroup.com

Date of Report: September 7, 2017

No proprietary or classified information, or any information subject to export control are included in this report.

DISCLAIMER

Executive Summary

This document is intended to give an overall synopsis of the activities and accomplishments of the EC Power CAEBAT2 project over the course of four years. The reader is referred to the previously submitted quarterly reports, review presentations, and AMR presentations for further technical details. As highlighted by the numerous results shown herein and the volume and quality of the publications and presentations made in the course of this project, we feel that we have made a strong impact in the community.

Table of Contents

Executive Summary ..... **i**

Table of Figures ..... **iv**

Table of Tables ..... **viii**

1. Introduction **1**

2. General model description **1**

Basic operating principles of a Li-ion battery *1*
Thermally coupled battery (TCB) model *4*
Governing equations *5*

3. Materials database **10**

4. Pack-level safety and abuse modeling **10**

5. Overcharge Modeling **15**

6. Cell Life Testing **20**

7. Cell Life Modeling and Validation **31**

8. Coupling of ECT3D with Structural Mechanics Model via Open Architecture Standard (OAS) **43**

9. Additional accomplishments from project **47**

Soft vs hard internal shorting during charging *48*
Safer cell structure for large EV cells *54*
Publications list *57*

10. Conclusions **59**

References **61**

Table of Figures

Figure 1. Schematic of a Li-ion battery, consisting of two porous electrodes with a separator in between. The whole cell is filled with liquid electrolyte. 3

Figure 2.Summary of the thermally-coupled battery (TCB) modeling approach. 5

Figure 3. Dependence of simulations on heat transfer coefficient for NCM/graphite 18650 cell at ambient and initial temperature of -25ºC; 1C discharge. 8

Figure 4: Schematic diagram of the hierarchy of three-grid method. Simulation domain is divided into three domains: thermal grid, electrode grid, and spherical grid for solid state diffusion. 9

Figure 5. Cell/pack nail penetration setup 11

Figure 6. Nail penetration mesh setup and simulation results for a single cell 12

Figure 7. Predicted current and voltage evolution for a single cell during nail penetration 12

Figure 8. Predicted and measured temperature evolution for a single cell during nail penetration 13

Figure 9. Nail penetration mesh setup and simulation results for a 3-cell pack 14

Figure 10. Predicted current and voltage evolution for a a 3-cell pack during nail penetration 14

Figure 11. Predicted and measured temperature evolution for a single cell during nail penetration 14

Figure 12. Experimental setup for battery overcharge test 16

Figure 13. Overcharge model calibrated against Sandia's overcharge experiments for all three cathode chemistries. 16

Figure 14. Experimental and predicted overcharge results for NCM at 45ºC with 1C charging current 17

Figure 15. Experimental and predicted overcharge results for NCM at -20ºC with 1C charging current 17

Figure 16. Experimental and predicted overcharge results for NCM at 45ºC with 10C charging current 18

Figure 17. Experimental and predicted overcharge results for NCM at -20ºC with 10C charging current 18

Figure 18. Experimental and predicted overcharge results for NCA at -20ºC with 1C charging current 19

Figure 19. Experimental and predicted overcharge results for NCA at 45ºC with 10C charging current 19

Figure 20. Experimental and predicted overcharge results for NCA at -20ºC with 10C charging current..... 20

Figure 21. Experimental procedures for cycle life studies..... 21

Figure 22. 3-electrode cell and setup..... 21

Figure 23. Separate contribution of positive/negative electrode to cell degradation measured by 3-electrode diagnostics..... 22

Figure 24. Cell performance curves for 2-electrode and 3-electrode cells..... 22

Figure 25. High energy and high power cell configuration..... 23

Figure 26. NMC111/C cell aging: capacity retention for high energy and high power cell at 25ºC..... 23

Figure 27. NMC111/C cell aging: performance for high energy and high power cell at 25ºC..... 24

Figure 28. NMC111/C cell aging: Impact of C-rate for high energy and high power cell at 25ºC..... 24

Figure 29. NMC111/C cell aging: Impact of temperature for high energy and high power cell..... 25

Figure 30. NMC111/C cell aging: EIS test for fresh high energy and high power cells..... 25

Figure 31. NMC111/C cell aging: EIS test for fresh and aged high energy cell..... 26

Figure 32. NMC111/C cell aging: Resistance vs cycle number extracted from EIS test for fresh and aged high energy cell..... 26

Figure 33. NMC111/C cell aging: EIS test for fresh and aged high power cell..... 27

Figure 34. NMC111/C cell aging: Resistance (extracted from EIS test) vs cycle number for fresh and aged high power cell..... 28

Figure 35. NMC622/C and NMC111 cell aging: performance for high energy cell at 23ºC 28

Figure 36. NMC622/C and NMC111 cell aging: capacity retention for high energy and high power cell..... 28

Figure 37. NMC622/C cell aging: Impact of C-rate for high energy cell at 25ºC..... 29

Figure 38. NMC622/C cell aging: Impact of temperature for high energy cell..... 29

Figure 39. NMC622/C cell aging: Impact of C-rate for high power cell at 25ºC..... 30

Figure 40. NMC622/C cell aging: Impact of temperature for high power cell..... 30

Figure 41. Flow chart of the new aging model and equations..... 32

Figure 42. NMC111/C cell aging: simulated capacity retention (25ºC, 1C charge/1C discharge cycle life)..... 32

Figure 43. NMC111/C cell aging: simulated capacity loss with and without crack propagation model (25ºC, 1C charge/1C discharge cycle life)..... 33

Figure 44. NMC111/C BOL performance: Model validation at different discharge C-rates for high power cell at 25ºC 33

Figure 45. NMC111/C BOL performance: Model validation at different discharge C-rates for high energy cell at 25ºC 34

Figure 46. NMC111/C BOL performance: Model validation at different temperatures for high power cell 34

Figure 47. NMC111/C BOL performance: Model validation at different temperatures for high power cell 35

Figure 48. NMC111/C BOL performance: Model validation at different discharge C-rates for high energy cell 35

Figure 49. NMC111/C BOL performance: Model validation at different temperatures for high energy cell 36

Figure 50. NMC111/C BOL performance: Model validation at different discharge C-rates for high power cell 36

Figure 51. NMC111/C BOL performance: Model validation at different temperature for high power cell 36

Figure 52. NMC622/C BOL performance: Model validation for high energy cell 37

Figure 53. NMC111/C life model validation: C/3 capacity retention for high energy cell ... 37

Figure 54. NMC111/C life model validation: C/3 discharge curves after various cycles for high energy cell 38

Figure 55. NMC622/C life model validation: C/3 discharge curves after various cycles for high energy cell 38

Figure 56. NMC6222/C life model validation: C/3 discharge curves after various cycles for high energy cell 39

Figure 57. NMC6222/C life model analysis: capacity loss in anode and cathode with/without crack propagation for high energy cell 39

Figure 58. NMC6222/C life model analysis: crack depth and lithium loss due to crack propagation for high energy cell 40

Figure 59. NMC622/C life model validation: C/3 discharge curves after various cycles for high power cell 40

Figure 60. NMC6222/C life model validation: C/3 discharge curves after various cycles for high power cell 41

Figure 61. NMC6222/C life model analysis: capacity loss due to SEI growth and crack propagation for high energy and high power cells 41

Figure 62. NMC6222/C life model analysis: maximum stress of each cycle for high energy and high power cells 42

Figure 63. NMC6222/C life model analysis: crack depth due to crack propagation for high energy and high power cells 42

Figure 64. Mesh for EC Power software and solidDisplacementFoam solver 44

Figure 65. Simulation results for 1C discharge at two time instants, t=2000s and 3500s. ... 44

Figure 66. Simulation results for 3C discharge at two time instants, t=600s and 1200s 45

Figure 67. Simulation results for 1C discharge at two time instants, t=2000s and 3500s for soft packaging 45

Figure 68. Simulation results for 3C discharge at two time instants, t=600s and 1200s for soft packaging 46

Figure 69. Simulation results for 1C discharge at two time instants, t=2000s and 3500s for rigid packaging 46

Figure 70. Simulation results for 3C discharge at two time instants, t=600s and 1200s for rigid packaging 47

Table of Tables

Table 1. Summary of the ECT3D governing equations..... 7

1. Introduction

At the outset of the CAEBAT project in 2013, our team had four primary goals, listed as follows:

- Develop an efficient pack-level safety and abuse model;
- Develop mechanism-based, fundamental models for accurately predicting degradation of Li-ion batteries under user-specified and wide-ranging temperatures and operating conditions;
- Perform co-simulation of our software with structural mechanics software via the Open Architecture Standard, developed by Oak Ridge National Laboratories;
- Perform testing and validate the cell and pack–level safety models and degradation models over wide-ranging temperature and operating conditions;
- Expand extensive materials database by experimentally characterizing and adding commercially-relevant cathode material, NCA, to our materials database.

Through the 3+ year effort of our team, we have accomplished all of these goals. This report gives a concise summary of these activities, and illustrates some of the R&D highlights from the team's activities.

2. General model description

Basic operating principles of a Li-ion battery

A Li-ion cell consists of three main components – a negative composite electrode (also known as the "anode"), separator, and a positive composite electrode (also known as the "cathode"). The basic cell structure and operating principle of a Li-ion battery is depicted in figure 1. For illustration purposes, a Li-ion battery with graphite (Li_xC_6) anode and iron phosphate (Li_yFePO_4) cathode is shown.

During discharge, Li^+ ions de-intercalate from Li_xC_6 solid particles in the negative electrode, travel through the liquid electrolyte across the separator into the positive electrode, and then intercalate into active material particles in the positive electrode, such as Li_yFePO_4. Electrons, blocked by the separator, are forced to travel an opposite route from Li^+ ions and pass through an external circuit. Electronic current is collected from the electrodes and sent to the battery terminals via a copper foil attached to the negative electrode and an aluminum foil attached to the positive electrode. During charging of the cell, the opposite process occurs, with Li^+ ions traveling from the positive electrode to the negative electrode, through the electrolyte. Full cells are built by either spirally winding long thin sheets into a cylindrical/prismatic shape or alternately stacking anode and cathode plates into prismatic shape.

The electrochemical reaction occurring at the solid/electrolyte interface of the negative electrode Li_xC_6 particles is

$$Li_x\ C_6 \underset{ch}{\overset{dis}{\rightleftharpoons}} Li_0\ C_6 + xLi^+ + xe^- \quad (1)$$

while the corresponding reaction at the solid/electrolyte interface of the positive electrode particles (e.g. $LiFePO_4$) is

$$FePO_4 + yLi^+ + ye^- \underset{ch}{\overset{dis}{\rightleftharpoons}} Li_y\ FePO_4 \quad (2)$$

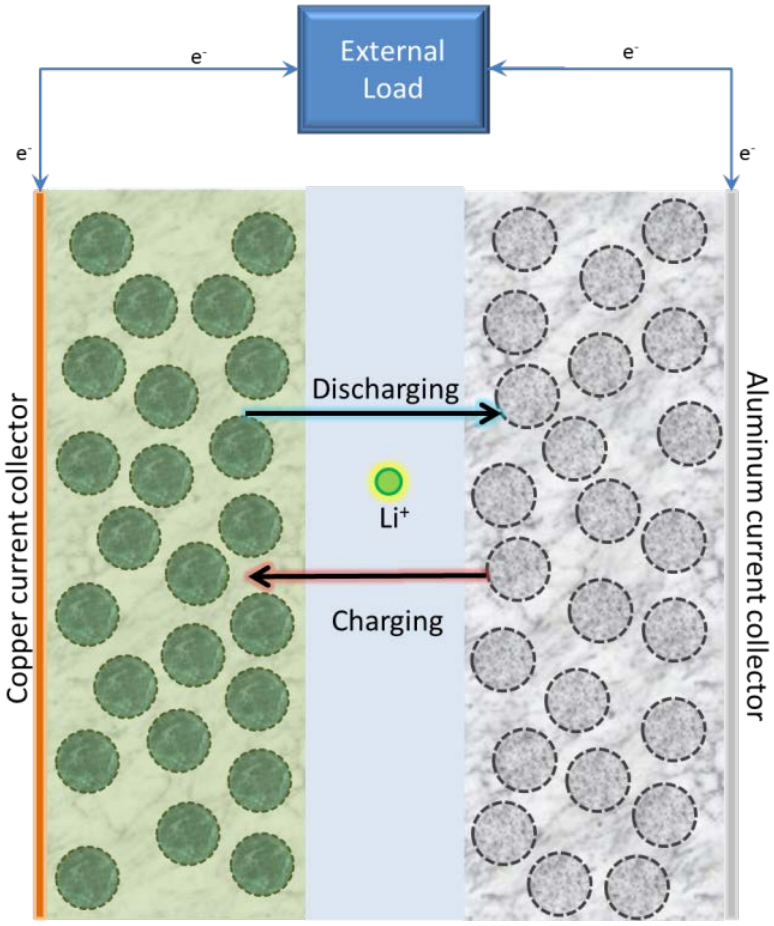

Figure 1. Schematic of a Li-ion battery, consisting of two porous electrodes with a separator in between. The whole cell is filled with liquid electrolyte.

As shown in figure 1, the electrodes are porous, with active material (solid particles) for storing the Li^+ ions. The solid particles are surrounded by either a liquid or gelled electrolyte solution responsible for transporting Li^+ ions across the separator to the opposite electrode. Cell performance during discharge and charge of Li-ion cells is dictated by kinetics of Li^+ intercalation/de-intercalation at active material particle surface, Li^+ diffusion inside solid particles, electrolyte transport under concentration gradients, and electron transport in the electrodes. Owing to inefficiencies associated with electrochemical reaction and transport processes, heat is generated during cell operation that needs to be effectively dissipated from cell surface during operation. As thermal feedback has a strong effect on the operating performance of Li-ion batteries – especially

large-format Li-ion batteries – properly modeling this thermal feedback is essential for capturing, for example operation in sub-freezing environments [2] and safety events that lead to thermal runaway [3]. These types of automotive applications necessitate a thermally-coupled battery (TCB) approach to modeling Li-ion batteries.

Thermally coupled battery (TCB) model

EC Power has developed the AutoLion™ software suite based on the electrochemical-thermal (ECT) coupled modeling approach that we refer to as thermally coupled battery (TCB) modeling. The TCB modeling approach has its roots in the isothermal model of Doyle and Newman [4], and substantial extensions through the electrochemically and thermal couplings by Gu and Wang [5], Srinivasan and Wang [6], and Smith and Wang [7]. The TCB modeling approach includes the following physico-chemical phenomena: Li intercalation/de-intercalation reactions at the electrode/electrolyte interface, transport of charge in both solid materials and electrolyte, transport of species (both neutral and ionic) by migration, diffusion and/or convection with the latter possibly induced by electrolyte flow due to electrode volume change, solid-phase Li diffusion in active materials, and thermal behaviors.

In a Li-ion battery, the thermal effects are strongly coupled with electrochemical processes. As shown in figure 2, the tight ECT coupling is a principal feature captured in AutoLion™ by the TCB modeling construct, and is critically important in being able to capture automotive-relevant simulations, such as the dynamics of cell shorting [3] and operation in subfreezing environments [2]. Figure 2 highlights how these two factors complement each other: the heat generated by the cell electrochemical processes feed directly into the thermal energy equation (via heat source term),

and as temperature changes, it feeds back into to the electrochemical process via the temperature-dependent, physico-chemical properties. The successful implementation of the TCB modeling construct in AutoLion^{TM} hinges on two critical factors: (1) an efficient and robust set of numerical algorithms to resolve strongly nonlinear couplings of the electrochemical and thermal equations, and (2) an accurate description of the battery's material properties over a wide range of conditions.

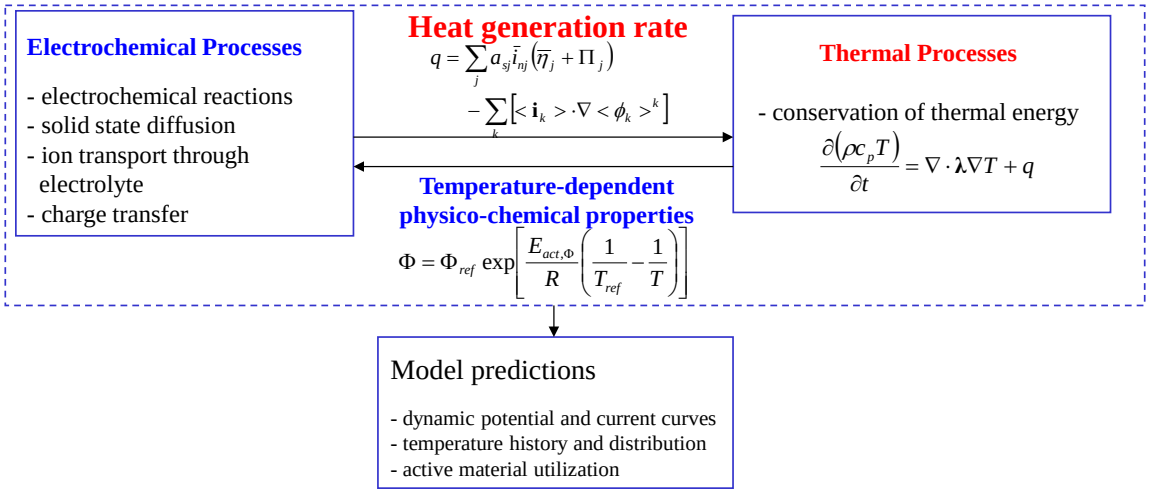

Figure 2.Summary of the thermally-coupled battery (TCB) modeling approach.

Governing equations

A brief summary of the ECT3D governing equations are given in table 1. The solid-phase conservation of charge, electrolyte-phase conservation of charge, and electrolyte-phase Li^+ species conservation equations are discretized in the three dimensions for the cell using a finite control volume approach. The active material Li species conservation equation is discretized in the radial direction of a representative active material particle. Further, in ECT3D, the energy equation is solved locally, as controlled by the macro thermal mesh, which includes discretization within the battery's anode/separator/cathode sandwich.

Using the TCB construct, there is no assumed or grossly approximated heat source. In the energy equation there are four heat sources: q_r is the reaction heat, q_j is the joule heat, q_c is the heat generation due to contact resistance, and q_e is the entropic heat. The reaction heat, joule heat, and entropic heat are calculated based on the local electrochemical conditions across the anode/separator/cathode sandwich; the local heat terms themselves are directly related to the output of the electrochemical equations, such as solid and electrolyte potential, and electrolyte concentration. The contact heat is determined from user-defined contact resistance of the given cell. The entropic heat is a thermodynamic property of the active cell materials, and is given by the materials database or user-input properties. For further details, the reader is referred to [10].

Butler-Volmer and Tafel equations, as appropriate, are used to model the reaction rates and the corresponding species source terms, j^{Li}, are given in table1. Note that in AutoLion™, there is no simplified treatment (e.g. linearized analytical or quasi-analytical solution) of solid diffusion in the active material particles. A numerical solution to the non-linear solid-phase diffusion equation (with $Ds = f(c_s,T)$) is performed.

AutoLion™ is largely based on the work of Gu and Wang [5], Wang and Srinivasan [6], Smith and Wang [7], and Fang et al. [10]. The reader should see these references for additional modeling details. One major benefit of AutoLion™'s TCB model as opposed to most Pseudo-2D or Newman-type models is that AutoLion™ utilizes a *fully coupled* electrochemical and thermal method. As a result, AutoLion™ can capture the voltage recovery period often seen in battery discharge from subfreezing temperatures. The TCB approach is also essential for the simulation of, for example, low-temperature operation of Li-ion batteries [2] and safety events [3]. Under

these conditions it is critical to account for the materials' strong coupling to temperature. This is highlighted in figure 3, which shows the discharge of an 18650 NCM/graphite cell at initial and ambient temperature of -25°C for several convection heat transfer coefficients, indicating different cooling conditions for the cell. It is evident from the figure that an isothermal model is incapable of predicting the voltage recovery that is observed under cell self-heating conditions, let alone the substantial differences in discharge performance for different heat transfer conditions.

Table 1. Summary of the ECT3D governing equations.

Description	Equation	
Solid-phase charge conservation	$\nabla.\left(\sigma^{eff}\nabla\phi_s\right)=j^{Li}$	(3)
Electrolyte-phase charge conservation	$\nabla.\left(k^{eff}\nabla\phi_e\right)+\nabla.\left(k_D^{eff}\nabla\ln C_e\right)=-j^{Li}$ $k_D^{eff}=\frac{2RTk^{eff}}{F}\left(t_+^0-1\right)\left(1+\frac{d\ln f_+}{d\ln C_e}\right)$	(4)
Electrolyte-phase Li^+ species conservation	$\frac{\partial}{\partial t}\left[\varepsilon c_e\right]=\nabla.\left(D_e^{eff}\nabla C_e\right)+\frac{1-t_+^o}{F}j^{Li}$	(5)
Active material Li species conservation	$\frac{\partial c_s}{\partial t}=\frac{1}{r^2}\frac{\partial}{\partial r}\left(D_s r^2\frac{\partial c_s}{\partial r}\right)$	(6)
Energy equation	$\frac{\partial}{\partial t}\left[\rho CT\right]=\nabla.\left(K\nabla T\right)+q_r+q_j+q_c+q_e$	(7)

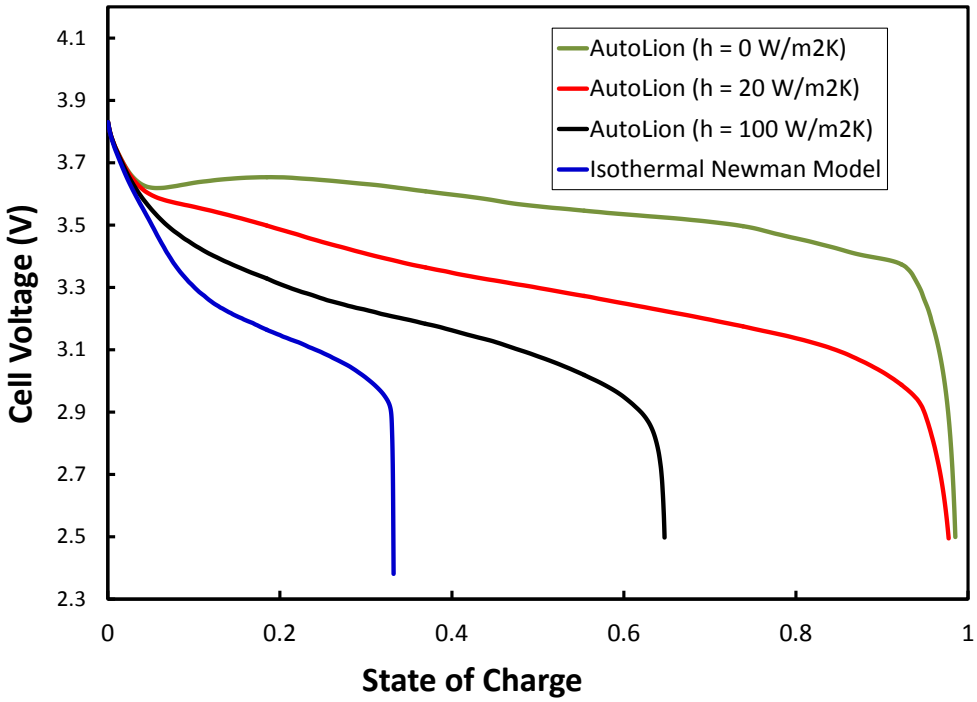

Figure 3. Dependence of simulations on heat transfer coefficient for NCM/graphite 18650 cell at ambient and initial temperature of -25°C; 1C discharge.

As shown in figure 4, in order to realize efficient simulation of large-format Li-ion batteries and packs, ECT3D employs a three-grid mesh, comprised of a macro-grid, a meso-grid, and a micro-grid. The thermal field (equation 7) is solved on the macro-grid, the electrochemical transport phenomena (equations 3, 4, 5) is solved on the meso-grid, and the solid-state diffusion inside active material particles (equation 6) is solved on the micro-grid. Note that there is one representative active material particle present within each meso-grid control volume, where active material is present (in the anode and cathode regions). With the TCB modeling construct there is a great deal of information passed between various grids. For example, the meso-grid calculations pass the rates of heat generation to the macro-grid, and the macro-grid passes the resulting temperature value to the meso-grid calculations. Further, the meso-grid model passes the reaction

current to the micro-grid, and micro-grid passes the surface concentration at the solid particle/electrolyte interface to the meso-grid.

The macro-grid takes into account all of the detailed geometries of components of the large-format cells and packs, including all coolant flow and related components in the battery pack. ECT3D internal algorithms automatically generate the meso and micro-grids from the macro-grid mesh with a simple zone numbering scheme outlined in the user guide. All the governing equations (equations 3 through 7) are solved at one time step. Equation 7 is solved by the CFD solver on the macro-grid level. Equations 3, 4, and 5 are solved on meso-grid level, and equation 6 is solved on the micro- grid level. All equations are solved using a finite-volume scheme. The thermal macro-grid mesh is generated by the user, to the appropriate resolution required by the cell and/or pack design. Using the AutoLion™ GUI, the user can specify the number of control volumes used in the macro- and micro-grid meshes. Further details of the user control are given in the user's guide, section.

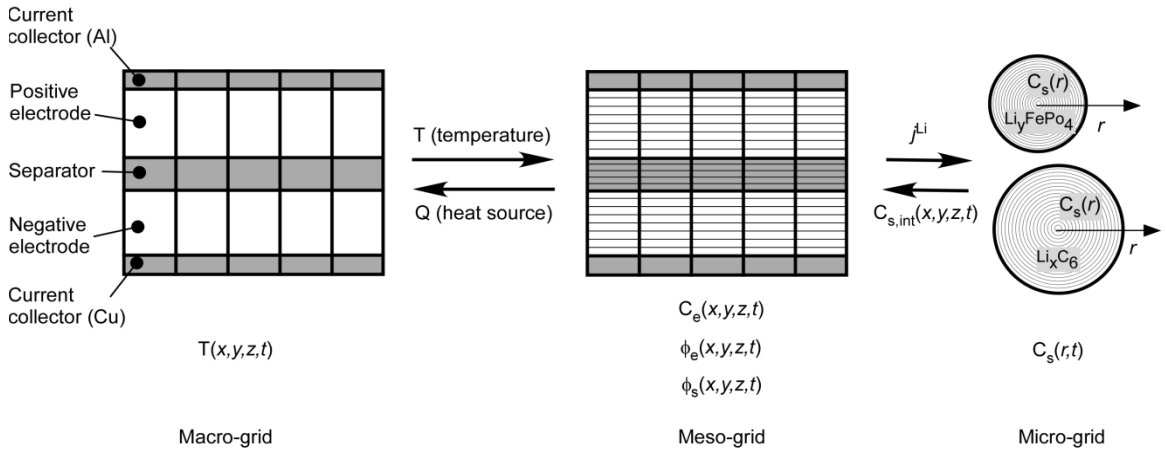

Figure 4: Schematic diagram of the hierarchy of three-grid method. Simulation domain is divided into three domains: thermal grid, electrode grid, and spherical grid for solid state diffusion.

3. Materials database

EC Power has developed and implemented in ECT3D an extensive materials database for a wide range of materials commonly used in commercial applications, such as $LiCoO_2$ (LCO), $LiFePO_4$ (LFP), $LiNi_{0.33}Mn_{0.33}Co_{0.33}O_2$ (NCM), $LiMn_2O_4$ (LMO) cathode materials, and graphite (LiC_6) and $Li_4Ti_5O_{12}$ (LTO) anode materials, in addition to electrolyte properties. The material properties have been measured as a function of temperature ($-30^oC < T < 60^oC$) and electrolyte concentration.

For this project, we completed characterizing commercially widely-used **NMC622** and **NCA** cathode materials ($-40^oC < T < 60^oC$) and added material properties to the previously developed extensive material database. We also added the anode material Si to the database after successful implementation of new performance and ageing model including effects of active material swelling.

4. Pack-level safety and abuse modeling

Li-ion cell safety is one of the biggest technological hurdles for the widespread use of large-format cells in automotive applications. ECT3D, owing to its thermally coupled battery modeling framework is ideally suited for comprehensive large-format cell safety simulations. Based on the previous version of ECT3D, which is capable of simulating full nail penetration, external short, and internal short in a cell with prismatic stacked electrode design, we have extended our safety capabilities to include a truly deterministic pack model safety simulation, where the user inputs nail/short properties, location, nail speed, etc., for a cell in the pack, and can use the tool to investigate how the safety event propagates though the pack both thermally and

electrochemically. Completed cell and pack level safety simulation capability make ECT3D an attractive tool to cell/pack abuse testing.

The first figure below outlines the cell/pack nail penetration experimental setup. The rest figures below illustrate results from the nail penetration process for single cell and 1S3P pack respectively. The validated simulation results reveal the reason that nail penetration of a 1S3P pack is much more dangerous than a single cell.

Figure 5. Cell/pack nail penetration setup

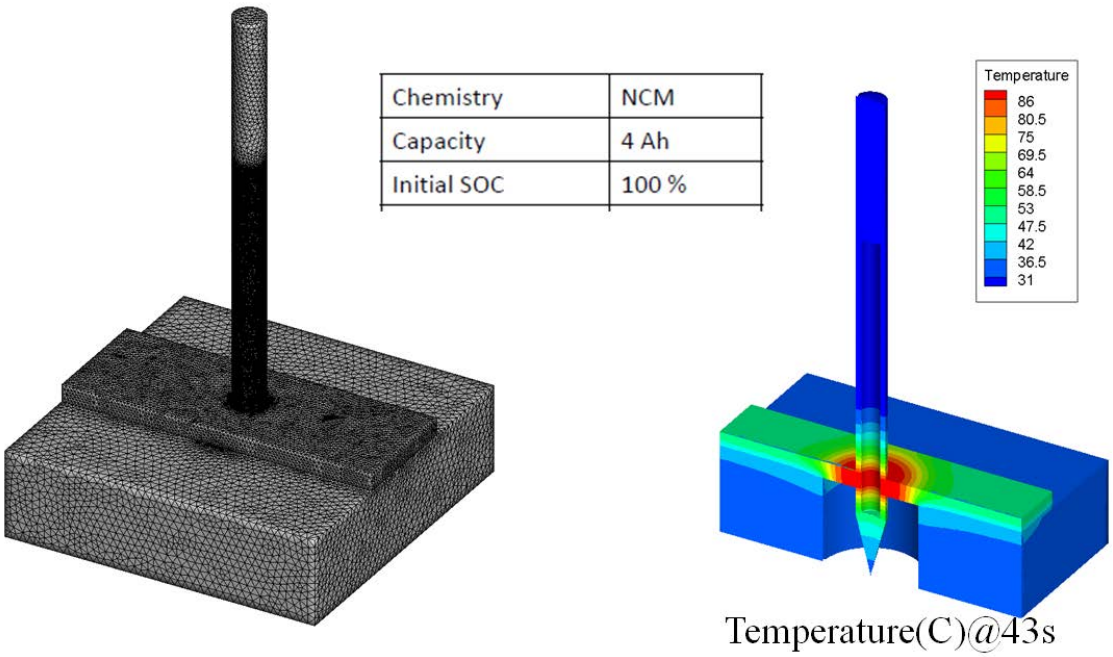

Figure 6. Nail penetration mesh setup and simulation results for a single cell

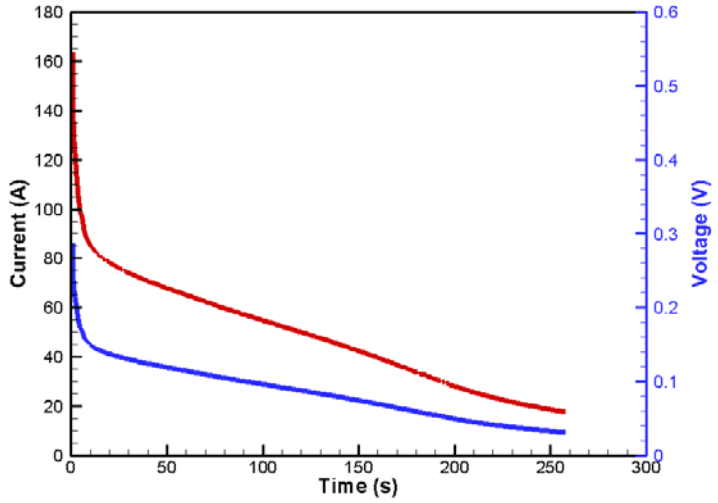

Figure 7. Predicted current and voltage evolution for a single cell during nail penetration

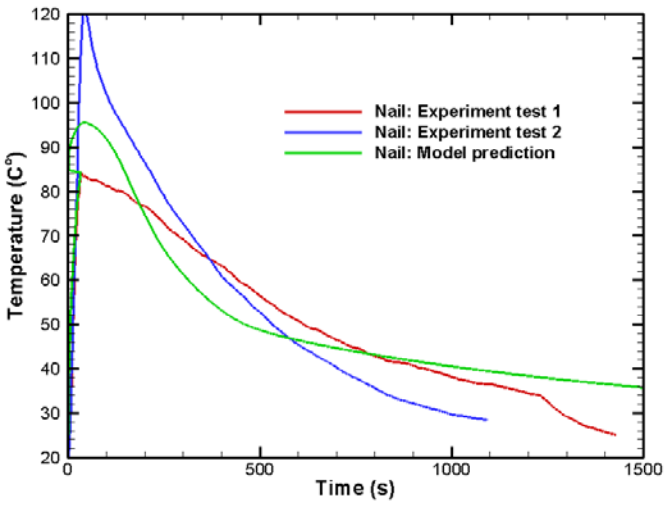

Figure 8. Predicted and measured temperature evolution for a single cell during nail penetration

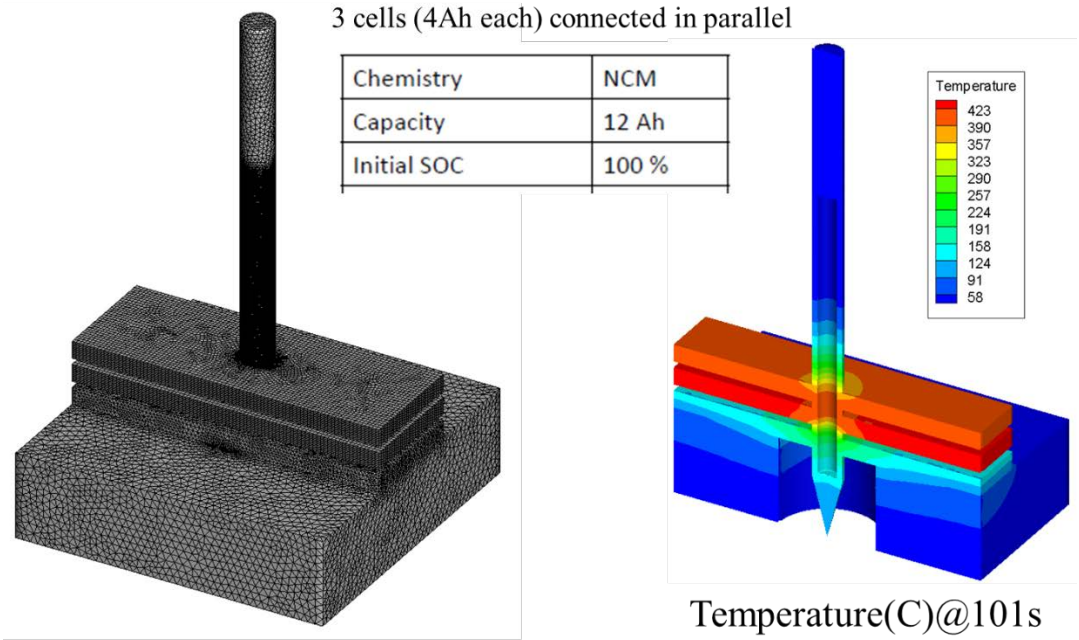

Figure 9. Nail penetration mesh setup and simulation results for a 3-cell pack

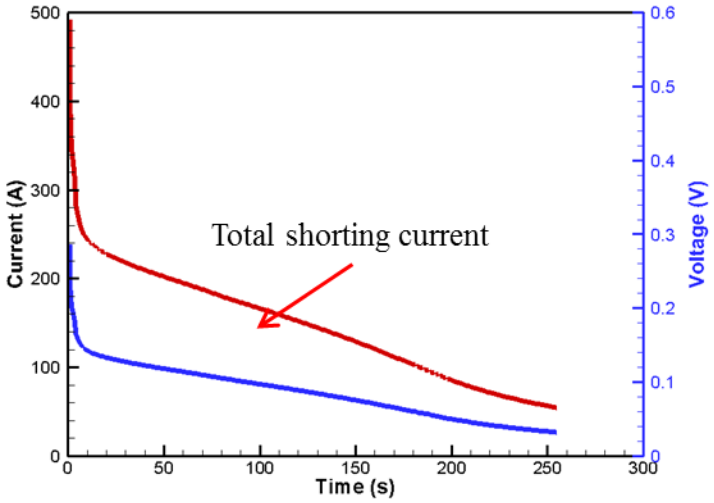

Figure 10. Predicted current and voltage evolution for a a 3-cell pack during nail penetration

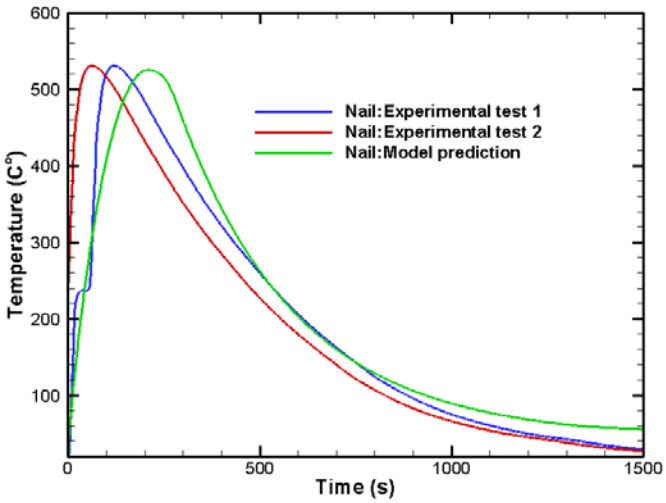

Figure 11. Predicted and measured temperature evolution for a single cell during nail penetration

5. Overcharge Modeling

Overcharge can occur if the control electronics of the battery management system (BMS) malfunction. It can also occur if there is severe cell imbalance in a battery pack. The thermal response of Li-ion cells during overcharge is largely determined by the cathode chemistry. Measurements of heat flow from the cells have shown that there is a rapid increase in heat generation when all of the lithium has been removed from the cathode. Overcharge may also cause plating of lithium in the graphitic anode, which not only leads to capacity loss but may also induce internal short-circuit due to the growth of lithium metal dendrite.

Safety associated with Li-ion cell overcharge is a very important issue for HEV and EV applications. Tolerance to overcharge depends strongly on charge rate and battery chemistry, particularly the cathode chemistry. During charge, cathode oxide material is delithiated. Different cathode materials have different residual stoich of Li at 100%SOC, e.g. $Li_{0.0}FePO_4$ and $Li_{0.48}Ni_{1/3}Co_{1/3}Mn_{1/3}O_2$. Further removing Li from cathode material may result in crystallographic changes in structure, releasing a large amount of heat and leading to cell thermal runaway. Overcharge of Li-ion cell triggers complex reactions, such as electrolyte decomposition and gas evolution, further leading to heat and pressure build-up within the overcharged cell. The present work simulates thermal and electrochemical consequences of overcharge. Two cells, NCM 2.0Ah and NCA2.8Ah, were tested at different charging rate and temperature. The experimental setup for all overcharge tests is shown in the first picture below. The rest are the experimental and model predicted results. Overcharge model of maximum temperature and temperature dynamics show good overall match with the experimental data.

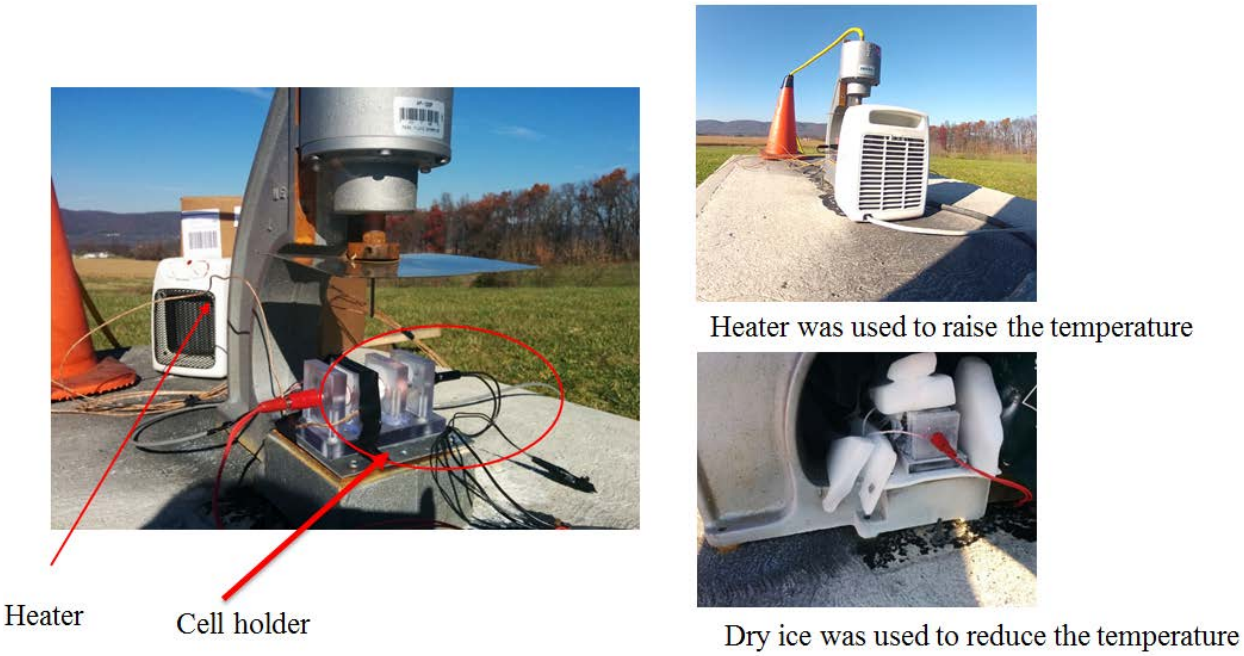

Figure 12. Experimental setup for battery overcharge test

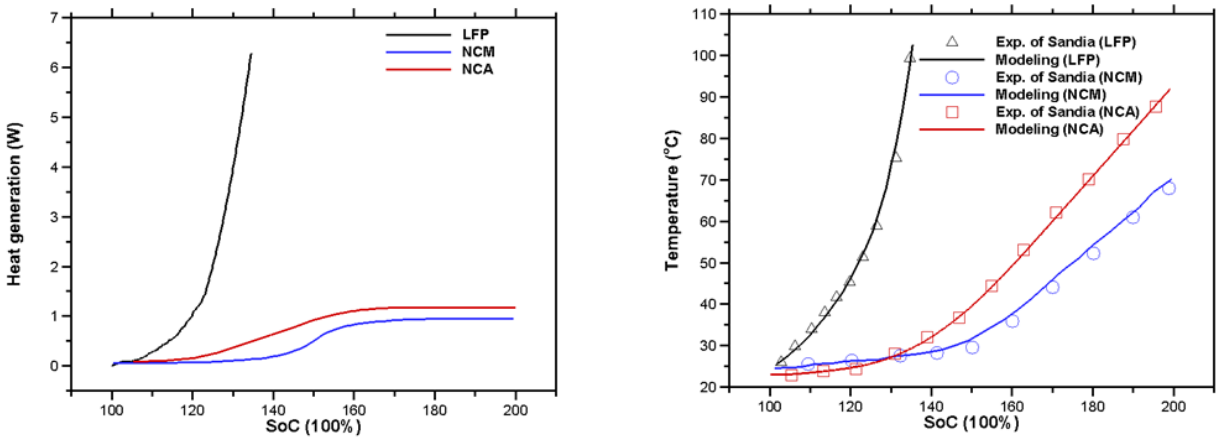

Figure 13. Overcharge model calibrated against Sandia's overcharge experiments for all three cathode chemistries.

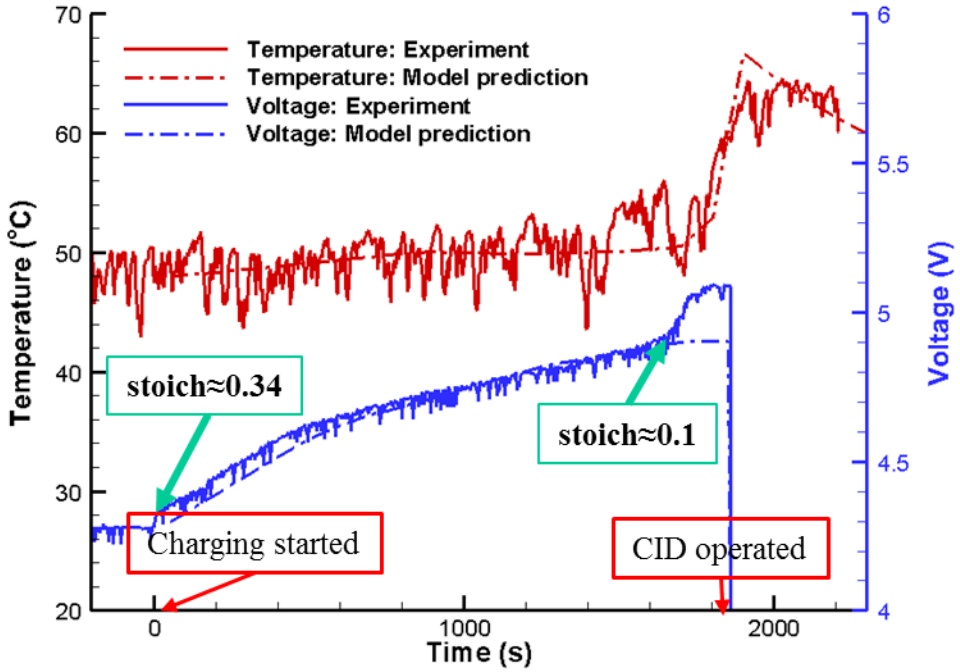

Figure 14. Experimental and predicted overcharge results for NCM at 45°C with 1C charging current

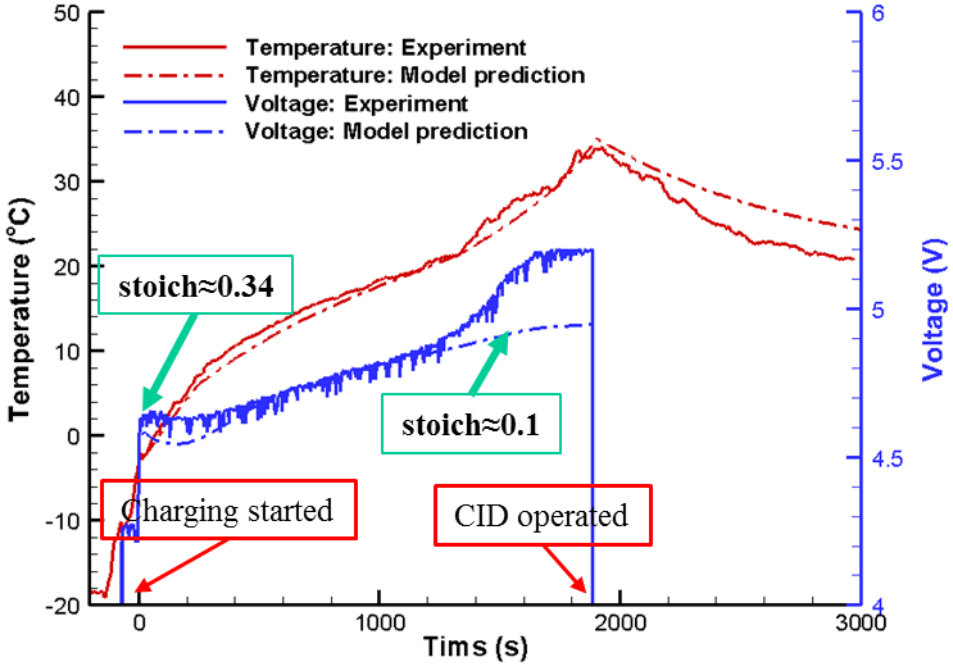

Figure 15. Experimental and predicted overcharge results for NCM at -20°C with 1C charging current

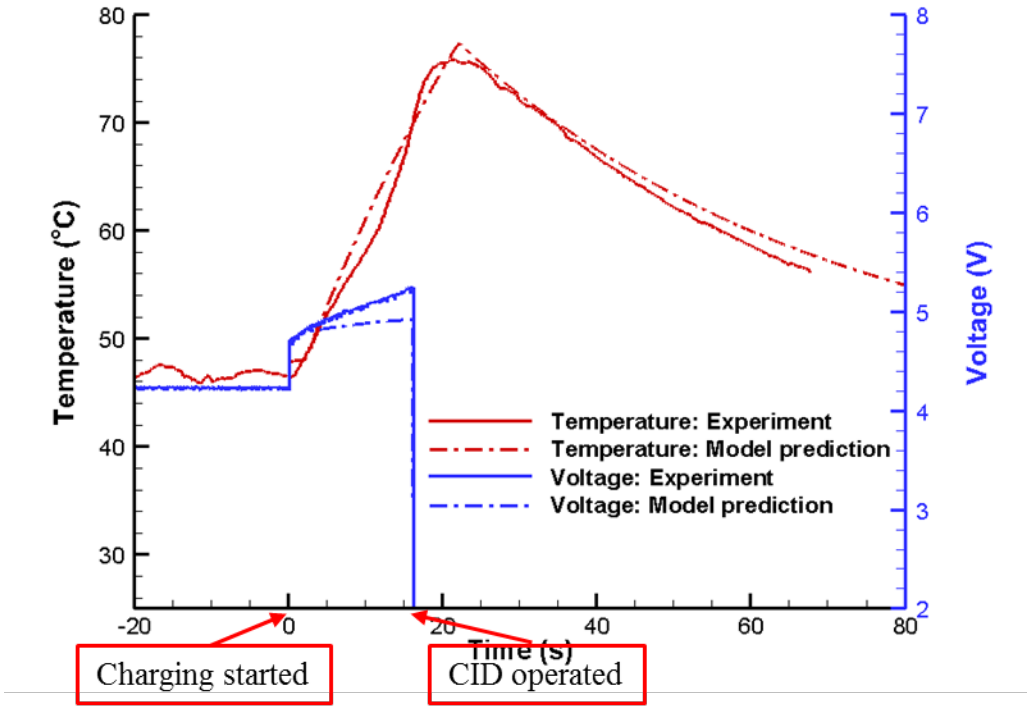

Figure 16. Experimental and predicted overcharge results for NCM at 45°C with 10C charging current

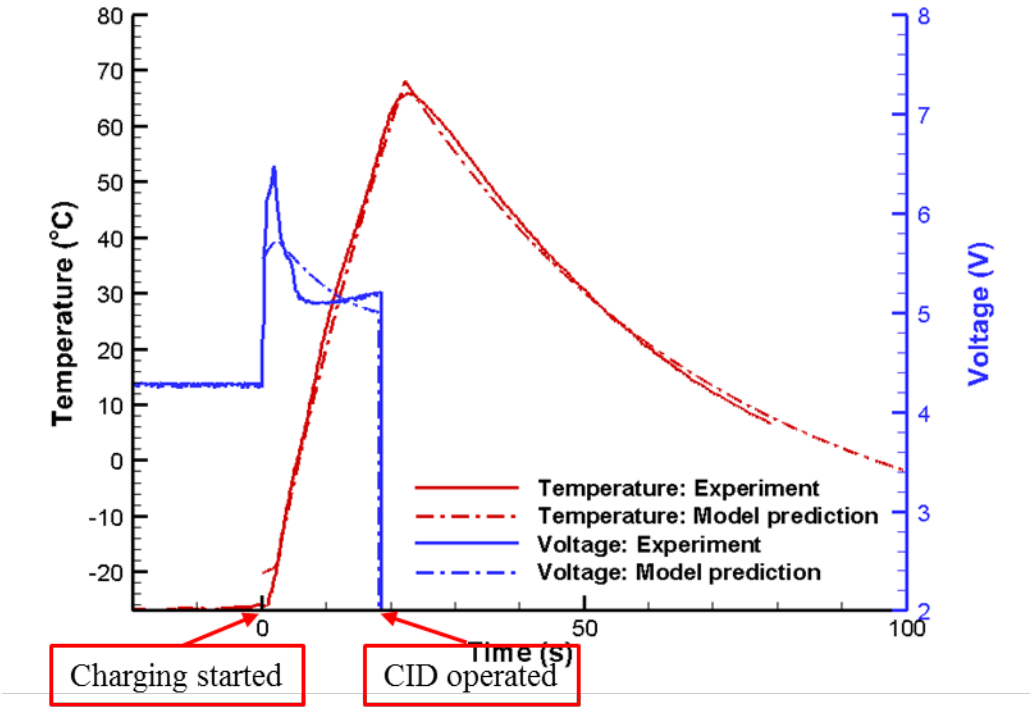

Figure 17. Experimental and predicted overcharge results for NCM at -20°C with 10C charging current

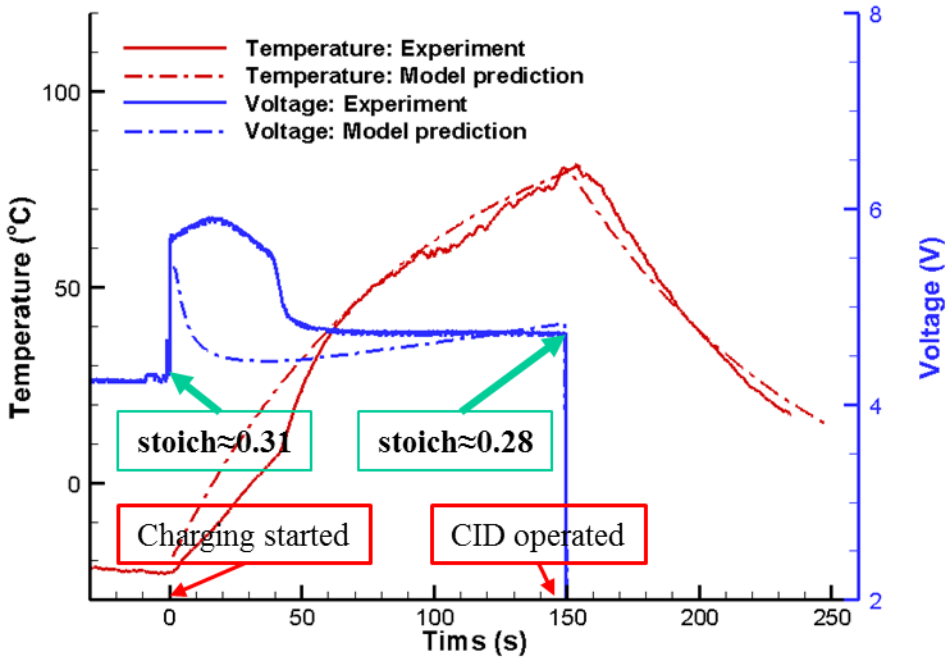

Figure 18. Experimental and predicted overcharge results for NCA at -20ºC with 1C charging current

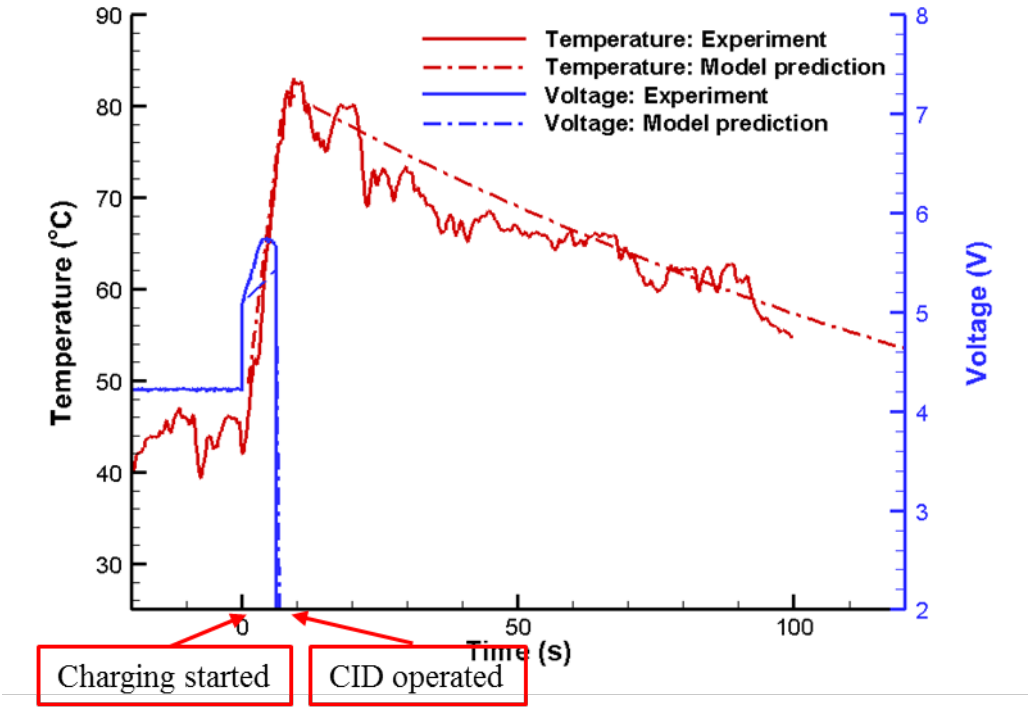

Figure 19. Experimental and predicted overcharge results for NCA at 45ºC with 10C charging current

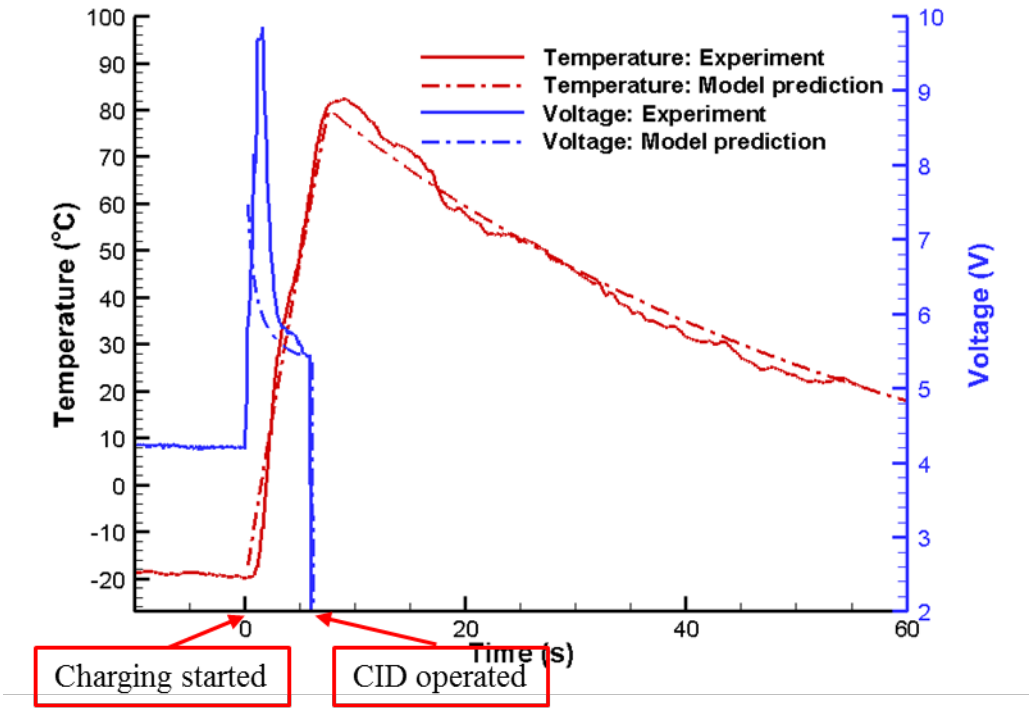

Figure 20. Experimental and predicted overcharge results for NCA at -20°C with 10C charging current

6. Cell Life Testing

Extensive cycling tests have been performed to collect data for NCM111 and NCM 622 cells for model validation. Testing procedures and setup are pictured in Figure 21 and 22. We used the 3-electrode cell to investigate the separate the contribution of positive/negative electrode to cell degradation. Li reference electrode works very well, as shown in Figures 23, 24. In order to identify degradation mechanisms of NMC/graphite cells and investigate the effect of electrode loading (or thickness) on cycle life, both high energy and high power cells are tested. The sketches and features for high energy and high power cells are list in Figure 25. For NCM 111 ($LiNi_{1/3}Co_{1/3}Mn_{1/3}O2$), mass capacity is 155 mAh/g rated at C/3. For NMC 622: ($LiNi_{0.6}Co_{0.2}Mn_{0.2}O2$), mass capacity is 172 mAh/g rated at C/3. The High energy cell has electrode mass loading ~20/12 (C/A) mg/cm^2. The High power cell has electrode mass loading ~10/6 (C/A) mg/cm^2.

The Figures 26 to 40 are the representative experimental testing results.

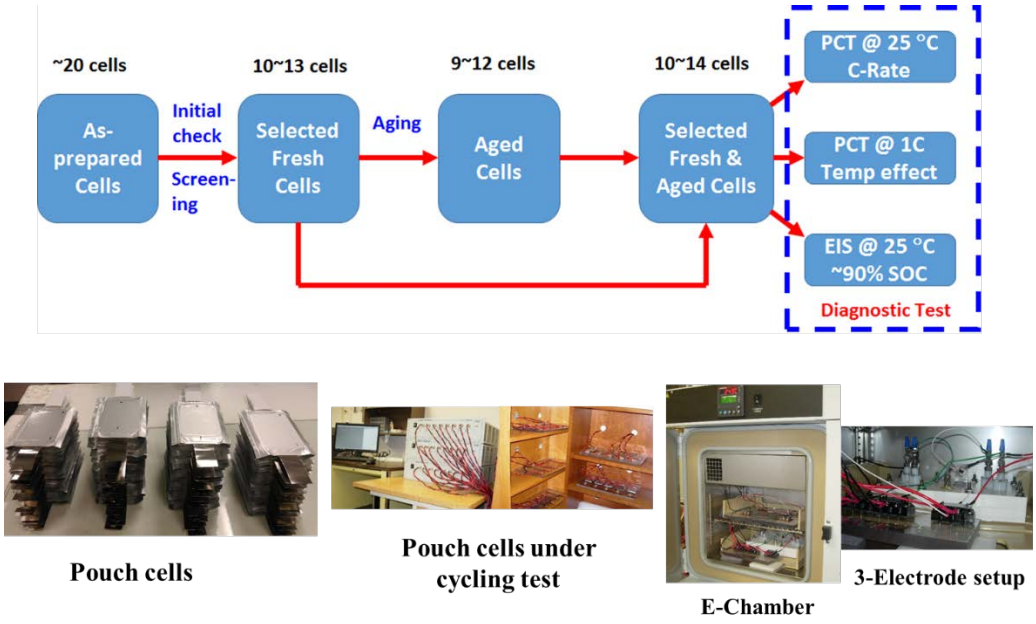

Figure 21. Experimental procedures for cycle life studies

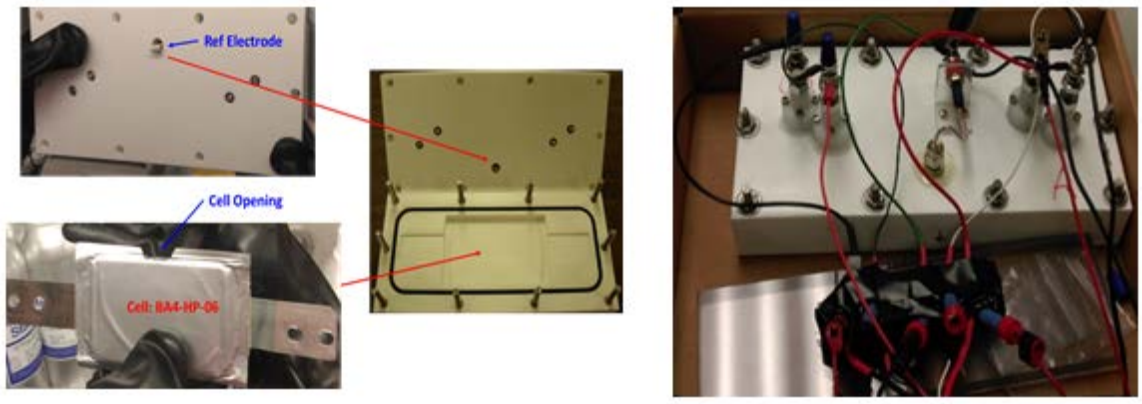

Figure 22. 3-electrode cell and setup

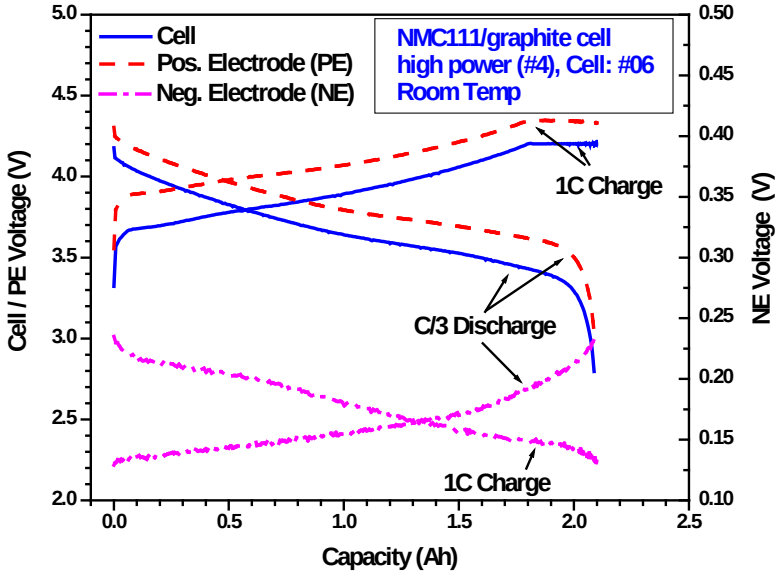

Figure 23. Separate contribution of positive/negative electrode to cell degradation measured by 3-electrode diagnostics.

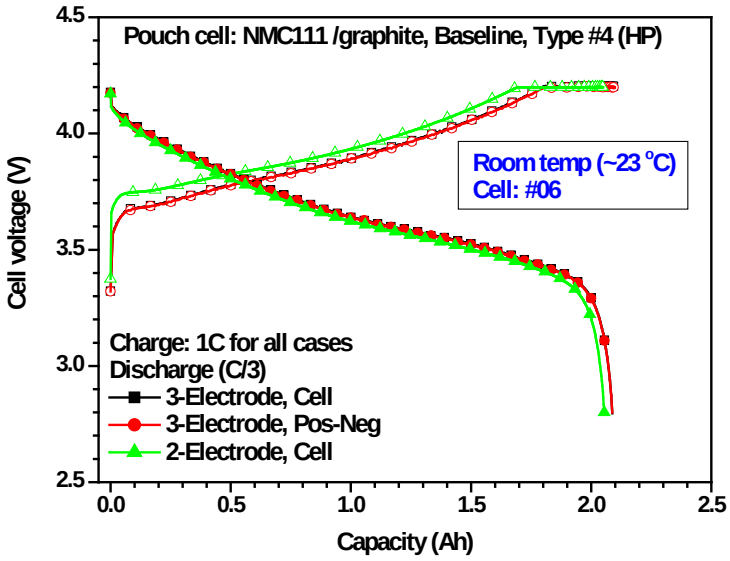

Figure 24. Cell performance curves for 2-electrode and 3-electrode cells.

Figure 25. High energy and high power cell configuration.

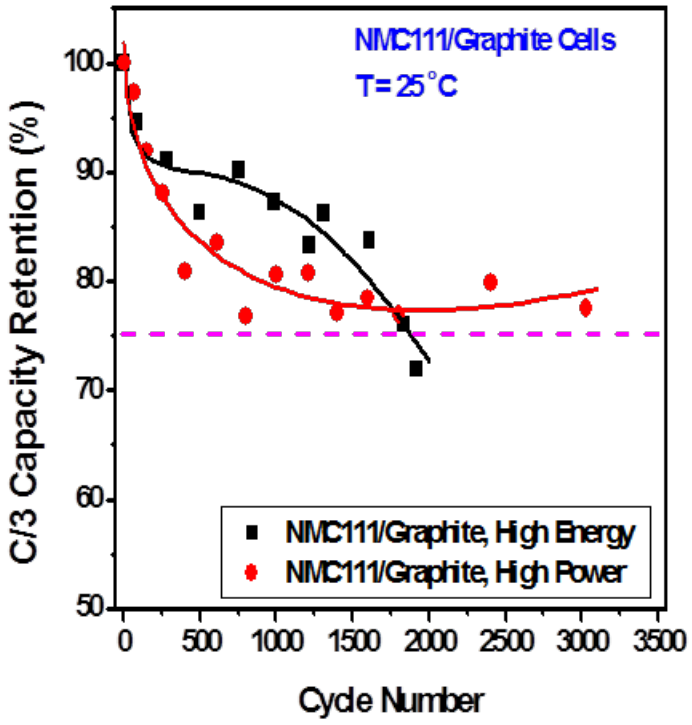

Figure 26. NMC111/C cell aging: capacity retention for high energy and high power cell at 25°C

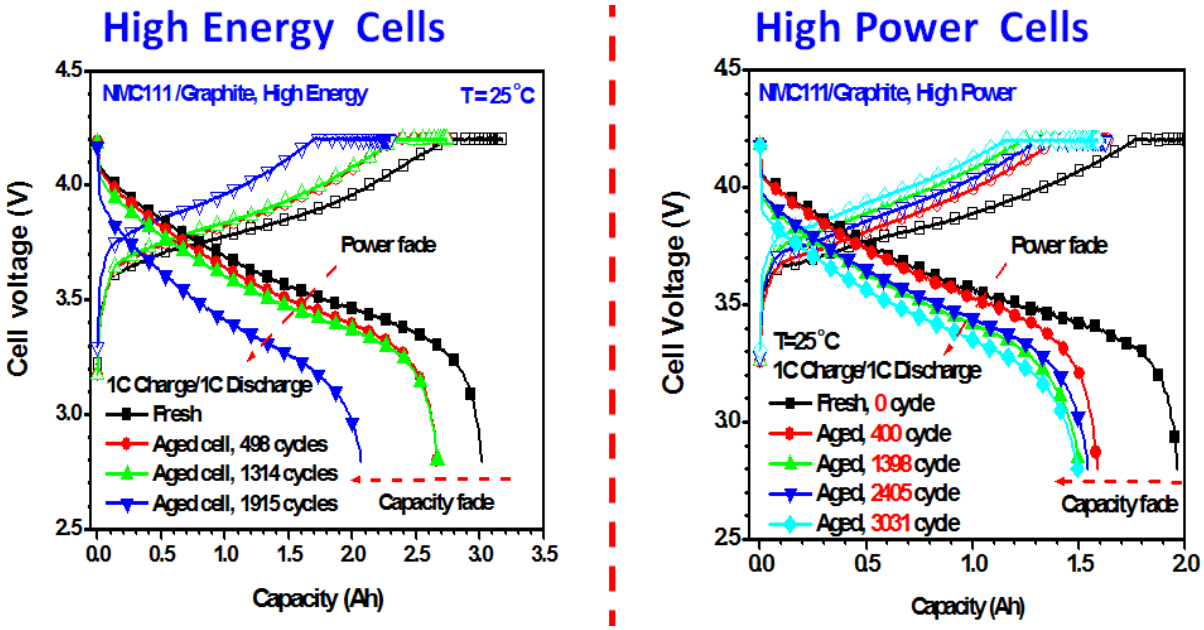

Figure 27. NMC111/C cell aging: performance for high energy and high power cell at 25°C

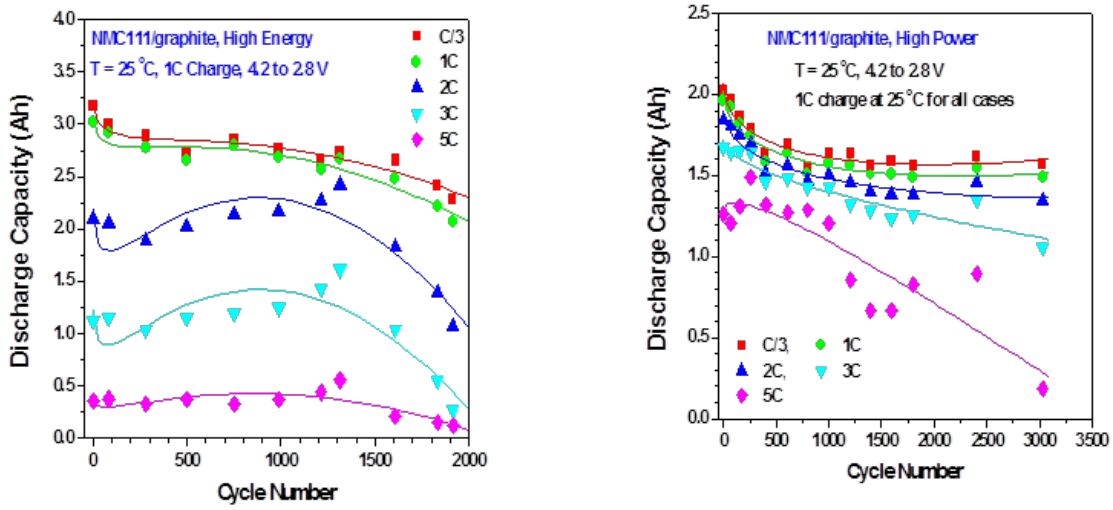

Figure 28. NMC111/C cell aging: Impact of C-rate for high energy and high power cell at 25°C

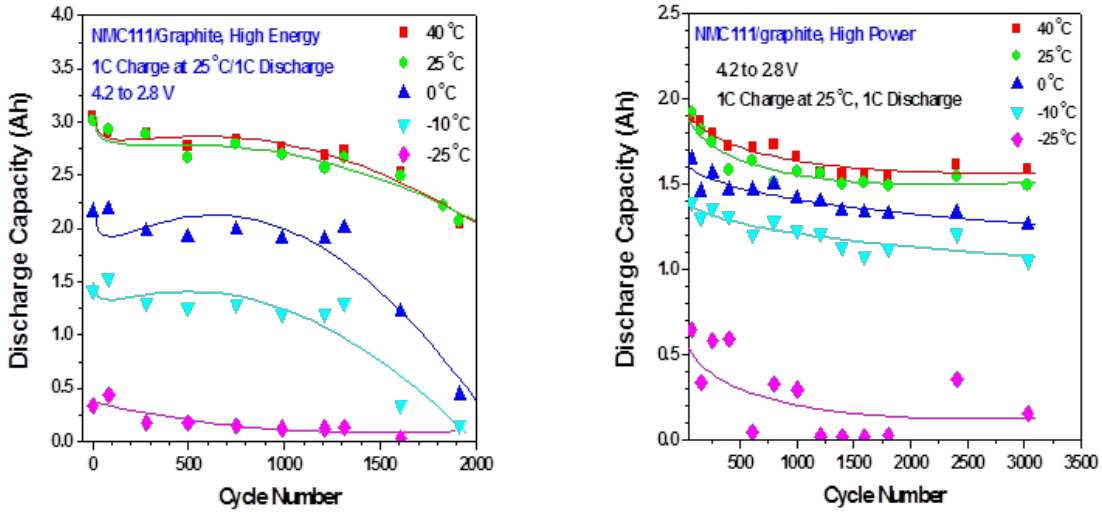

Figure 29. NMC111/C cell aging: Impact of temperature for high energy and high power cell

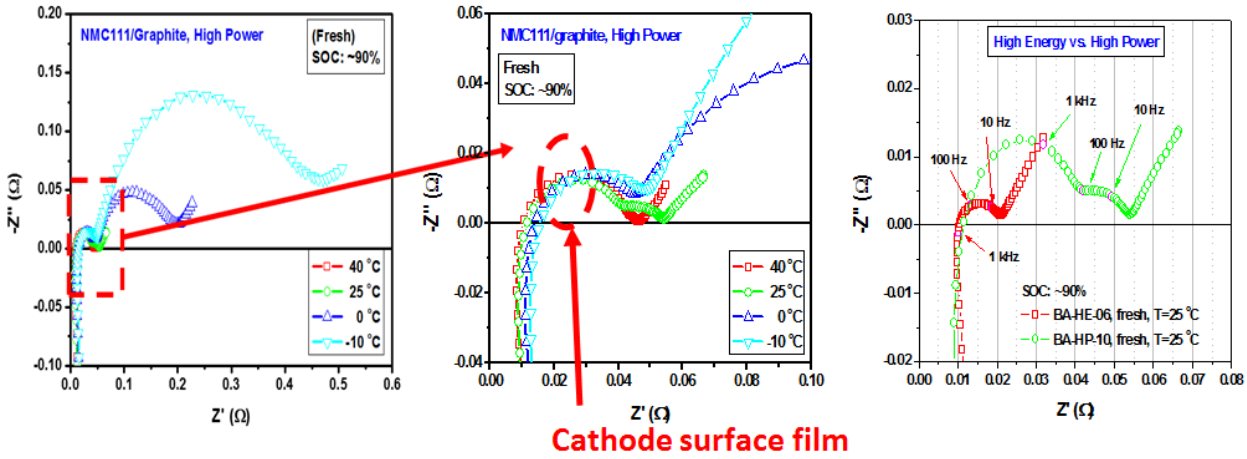

Figure 30. NMC111/C cell aging: EIS test for fresh high energy and high power cells

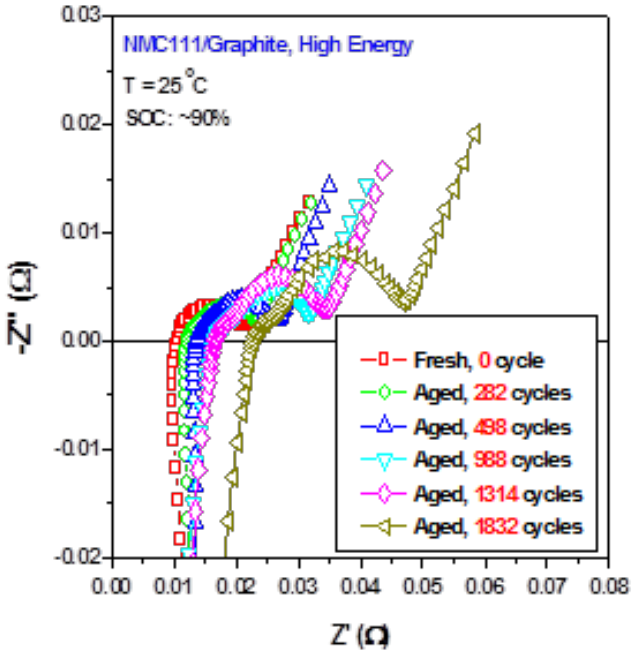

Figure 31. NMC111/C cell aging: EIS test for fresh and aged high energy cell

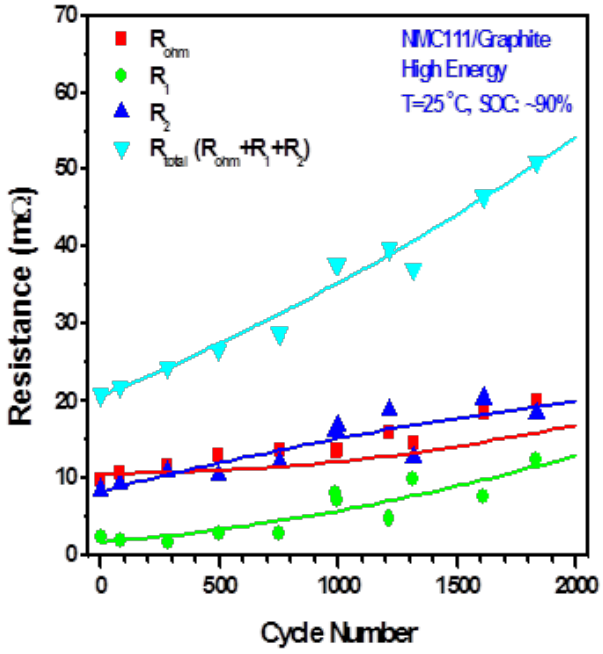

Figure 32. NMC111/C cell aging: Resistance vs cycle number extracted from EIS test for fresh and aged high energy cell

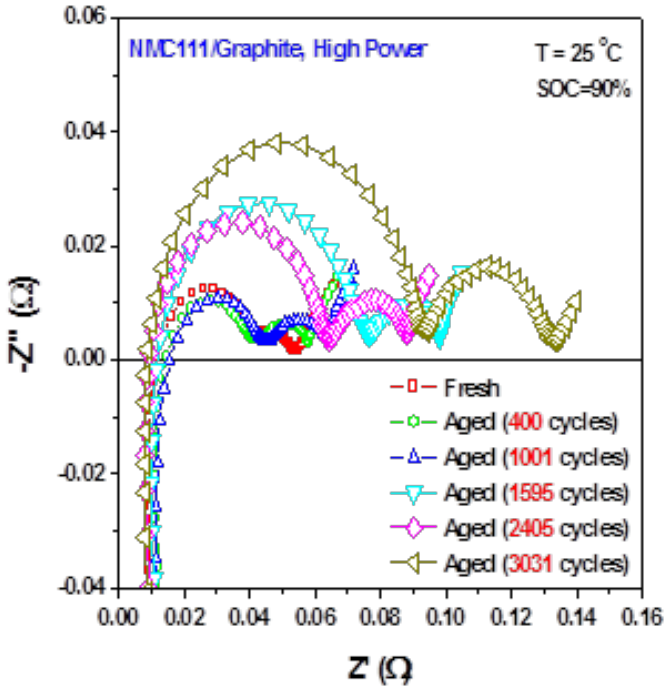

Figure 33. NMC111/C cell aging: EIS test for fresh and aged high power cell

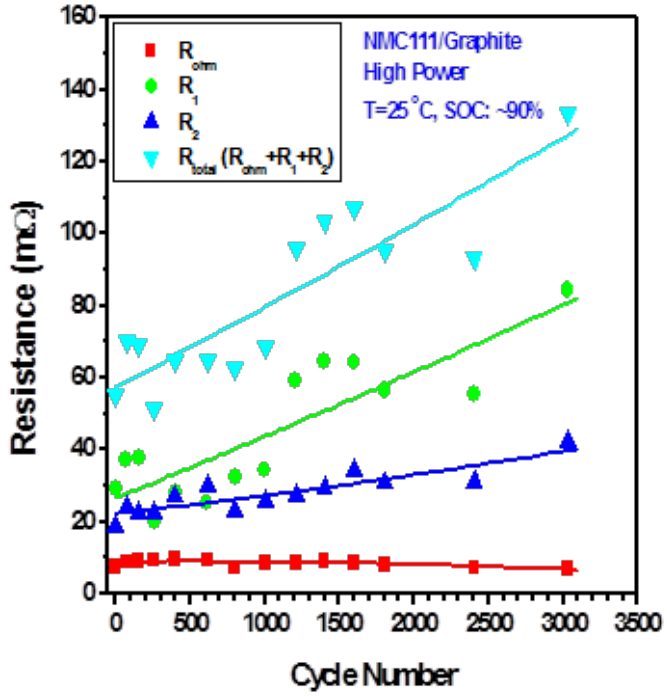

Figure 34. NMC111/C cell aging: Resistance (extracted from EIS test) vs cycle number for fresh and aged high power cell

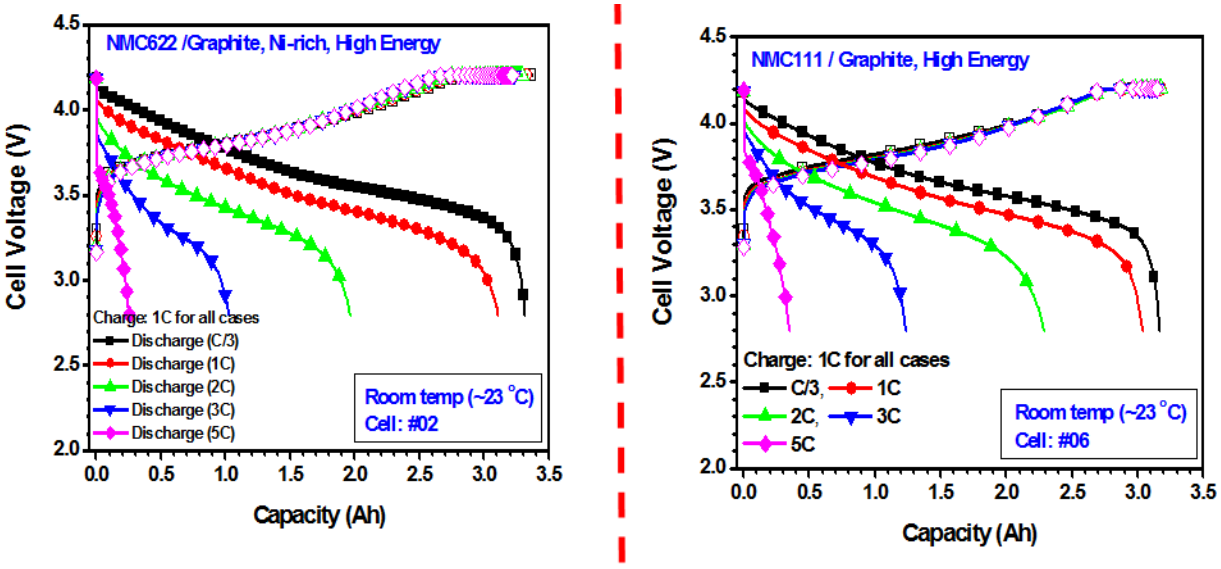

Figure 35. NMC622/C and NMC111 cell aging: performance for high energy cell at 23ºC

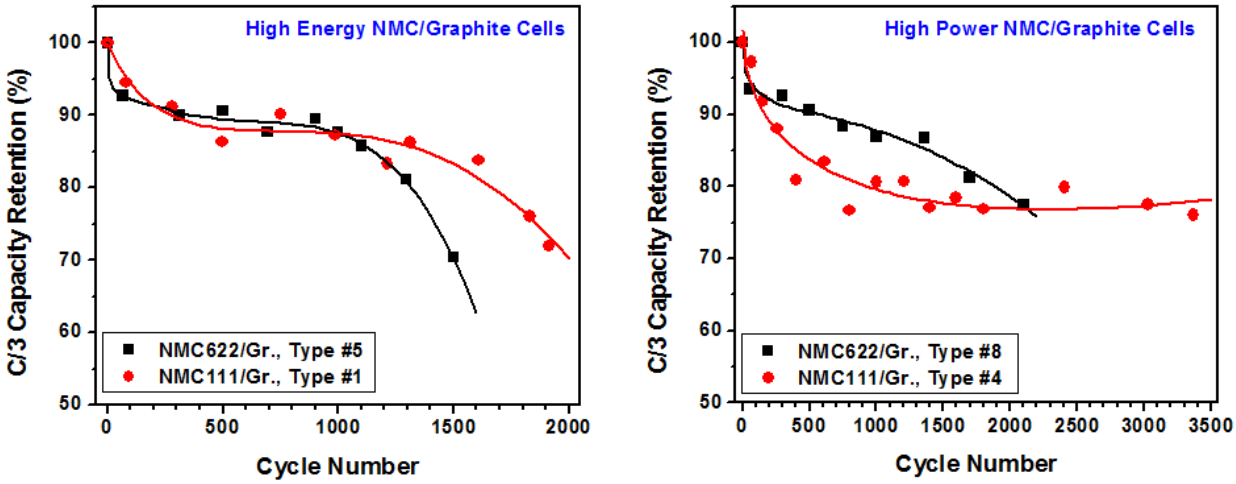

Figure 36. NMC622/C and NMC111 cell aging: capacity retention for high energy and high power cell

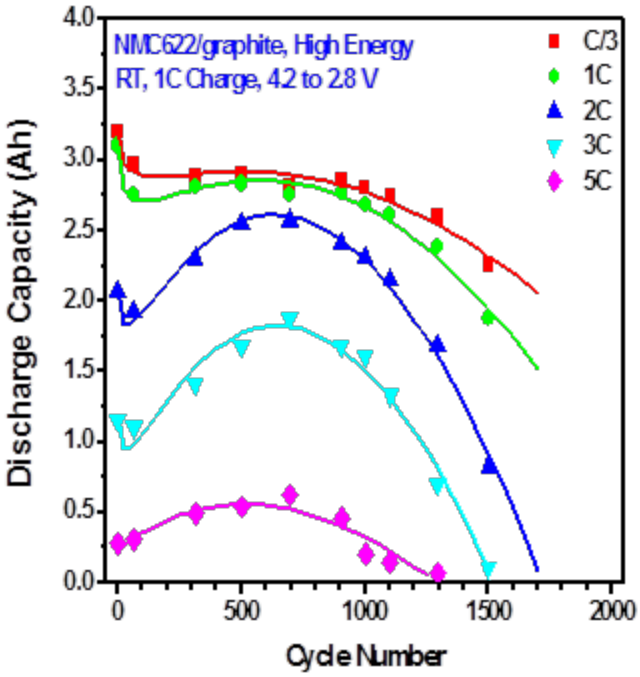

Figure 37. NMC622/C cell aging: Impact of C-rate for high energy cell at 25ºC

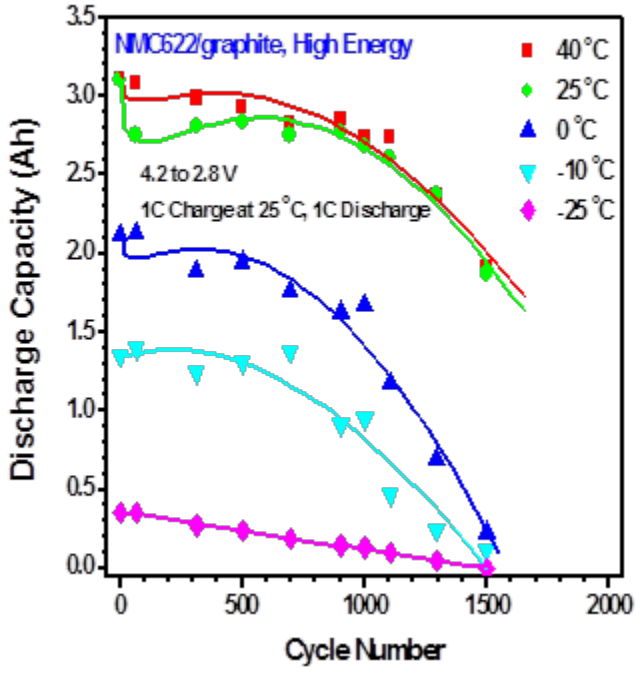

Figure 38. NMC622/C cell aging: Impact of temperature for high energy cell

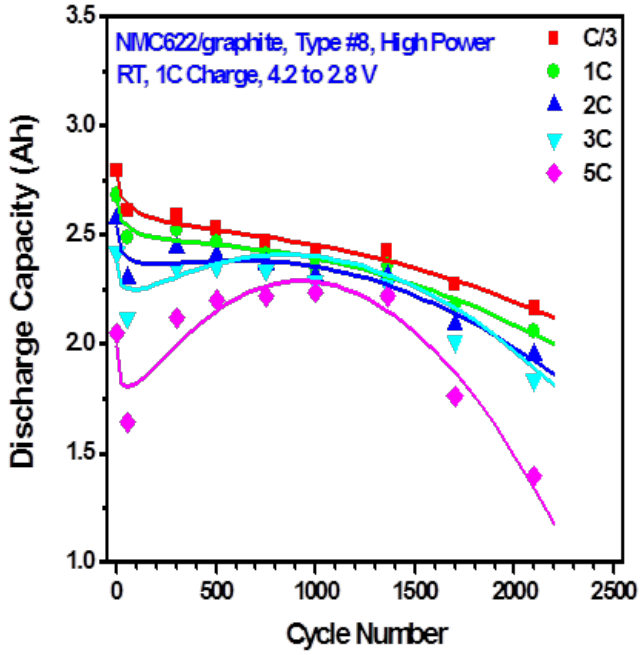

Figure 39. NMC622/C cell aging: Impact of C-rate for high power cell at 25ºC

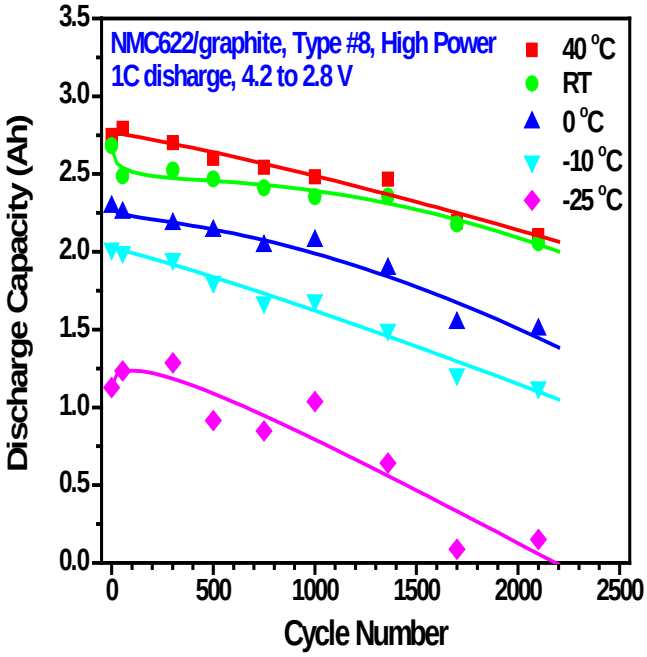

Figure 40. NMC622/C cell aging: Impact of temperature for high power cell

7. Cell Life Modeling and Validation

The AutoLion Cycle life modeling frame work includes the SEI growth on anode, film growth on cathode, and active material isolation (detaching away from binder/filler matrix) on both anode and cathode. As active material particle swell and shrink with lithiation, active material particles cracks with cycling. This aging mechanism was not considered in the current frame work. Thus, in this work we have incorporated electrode structure degradation (ESD) and its dependence on electrode loading or thickness. In this model, we assume that stress formation and development in thick electrodes, causing crack propagation in graphite particles. Lithium is lost due to formation of SEI layers on the newly cracked surfaces [11].

Figure 41 show the governing equations and flow chart for the model. Our new model of degradation starts from prediction of stress evolution during battery cycling, estimation of crack propagation and the ensuing area of newly exposed surfaces, and then followed by determination of loss of active cyclable lithium. Representative comparisons of the model prediction with charge-discharge performance at the beginning of life are shown in Figure 44 to 52 for NCM111/C and NCM622/C (high energy and high power) cells. Excellent agreement is found under a wide range of operating conditions. Figures 53 to 63 depict experimental validation of the new degradation model against NCM111/C and NCM622/C (high energy and high power) cell data. Again, good agreement is achieved in cycle life model validation.

This model along with previously developed SEI layer model and oxide film growth model gives rise to a comprehensive degradation model that can predict the electrode thickness effect on battery cycle life.

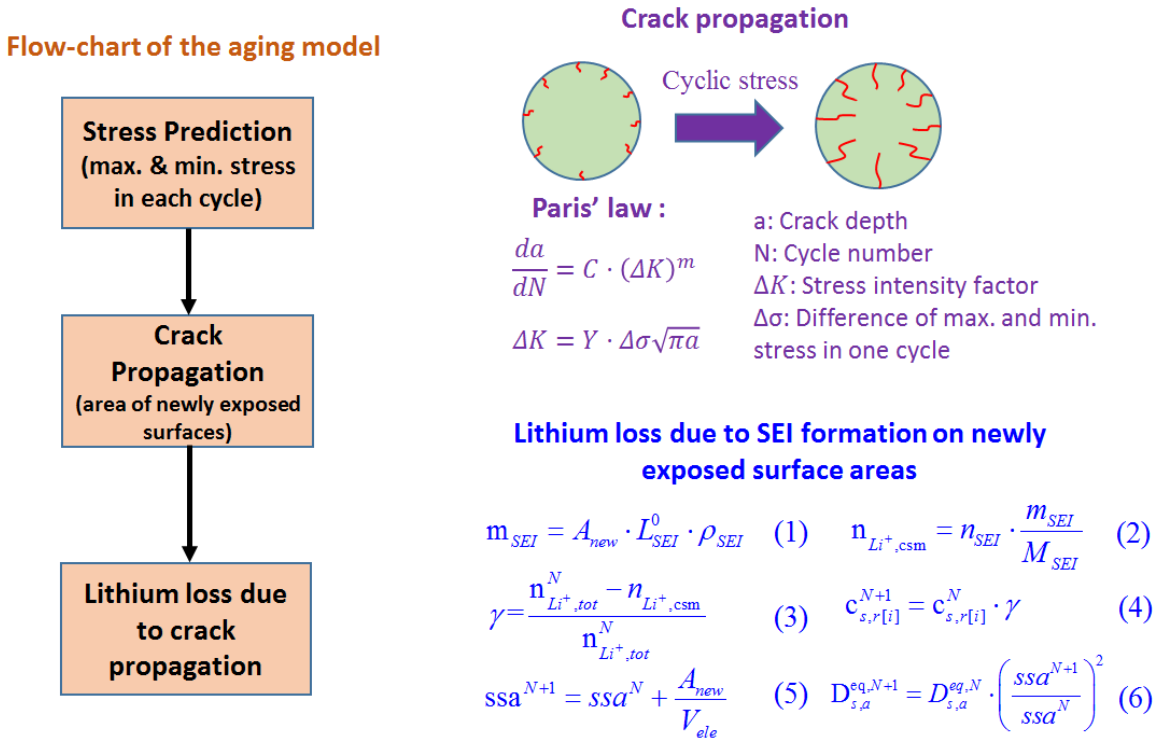

Figure 41. Flow chart of the new aging model and equations

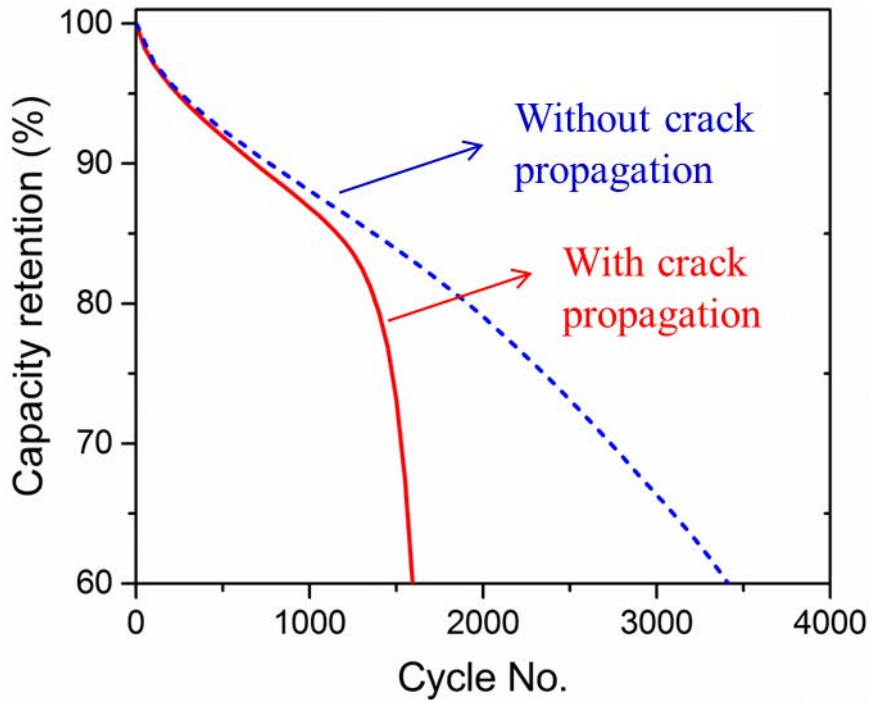

Figure 42. NMC111/C cell aging: simulated capacity retention (25°C, 1C charge/1C discharge cycle life)

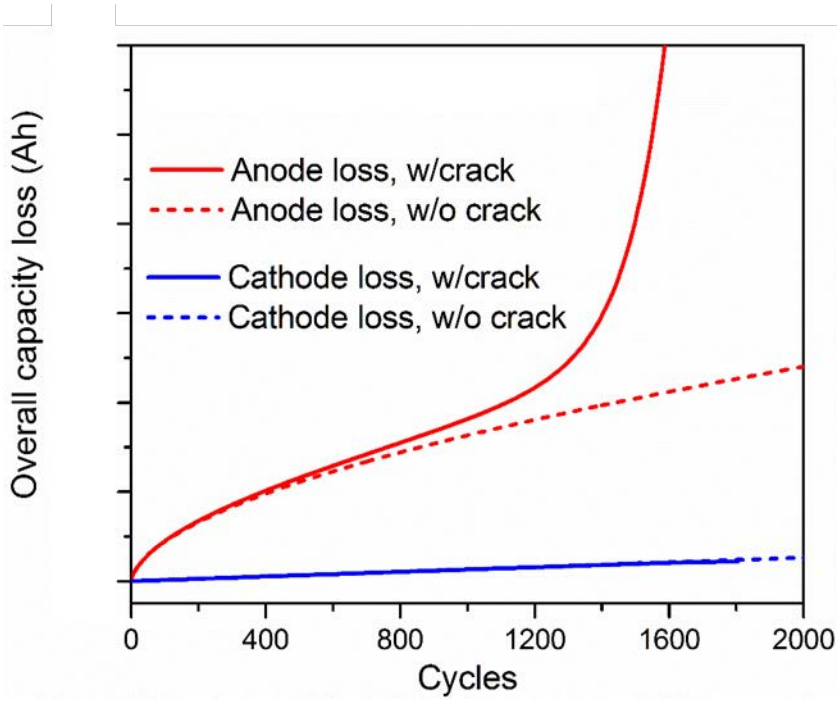

Figure 43. NMC111/C cell aging: simulated capacity loss with and without crack propagation model (25ºC, 1C charge/1C discharge cycle life)

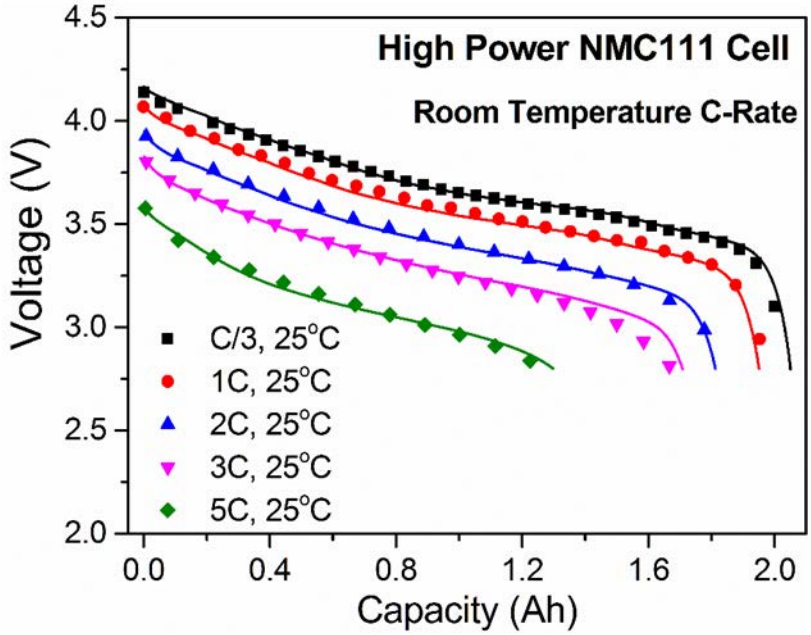

Figure 44. NMC111/C BOL performance: Model validation at different discharge C-rates for high power cell at 25ºC

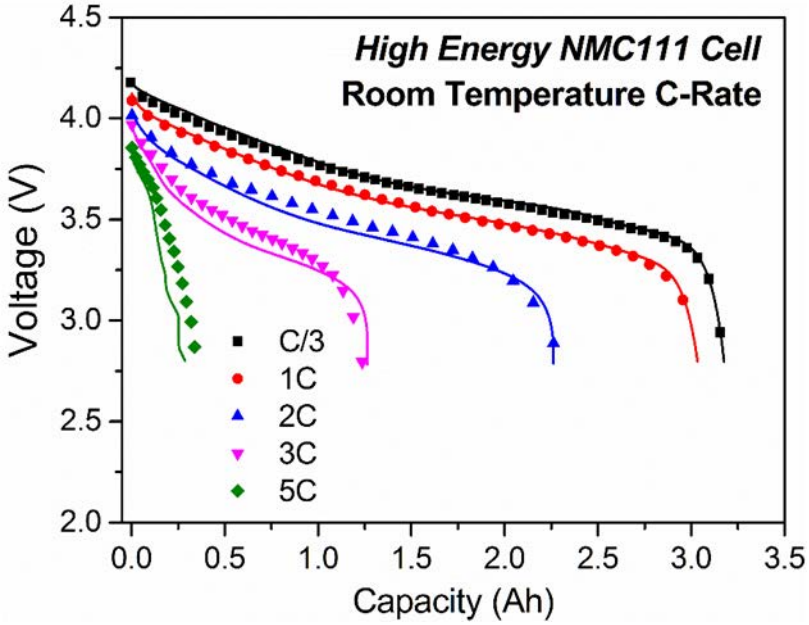

Figure 45. NMC111/C BOL performance: Model validation at different discharge C-rates for high energy cell at 25ºC

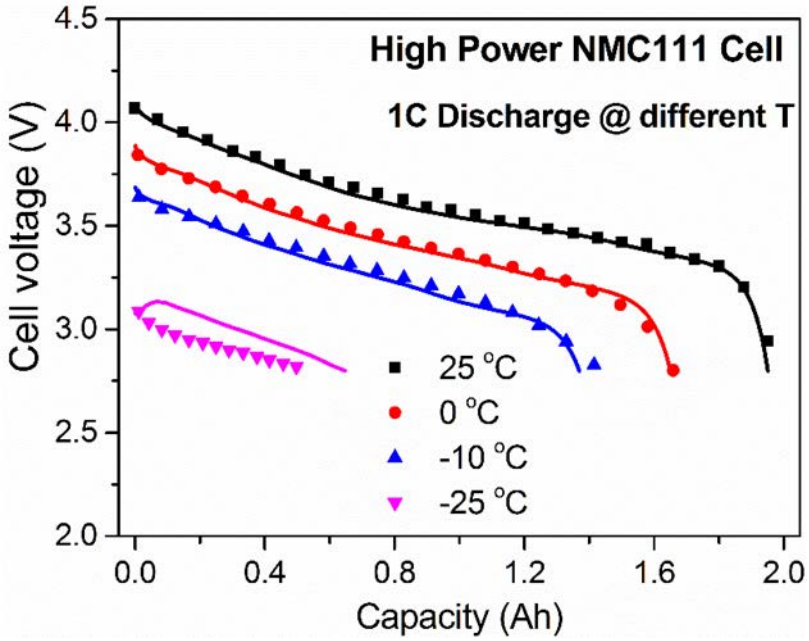

Figure 46. NMC111/C BOL performance: Model validation at different temperatures for high power cell

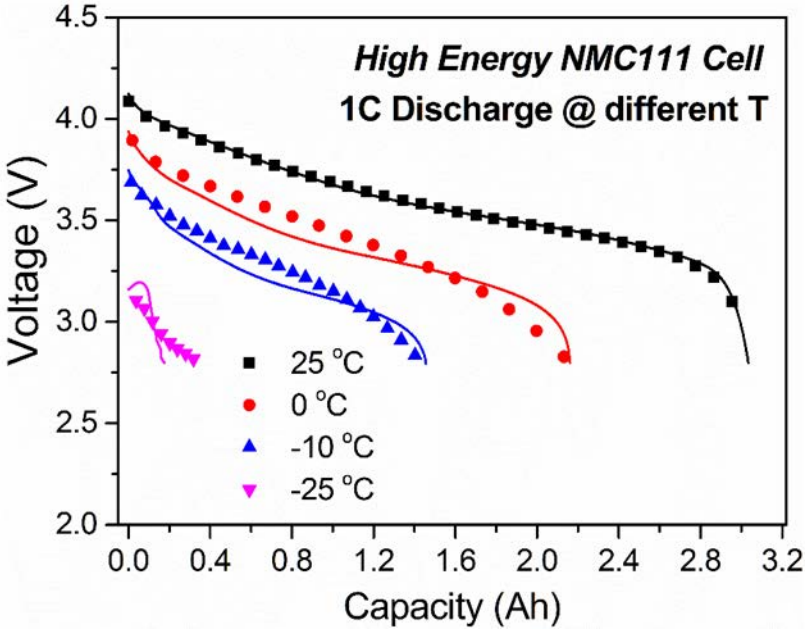

Figure 47. NMC111/C BOL performance: Model validation at different temperatures for high power cell

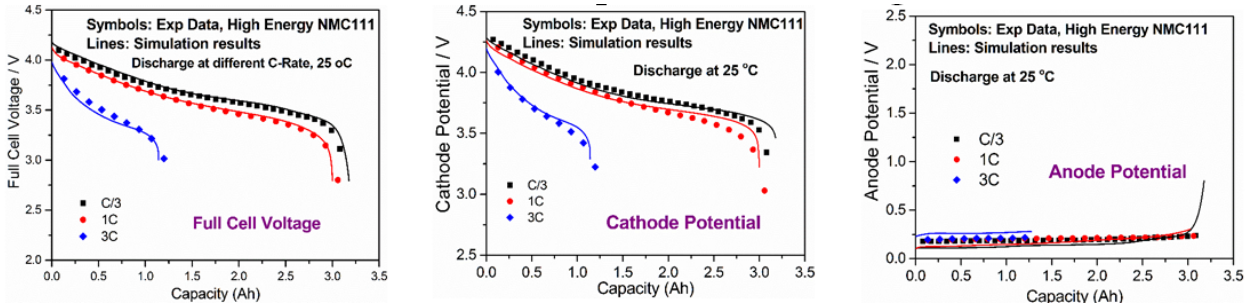

Figure 48. NMC111/C BOL performance: Model validation at different discharge C-rates for high energy cell

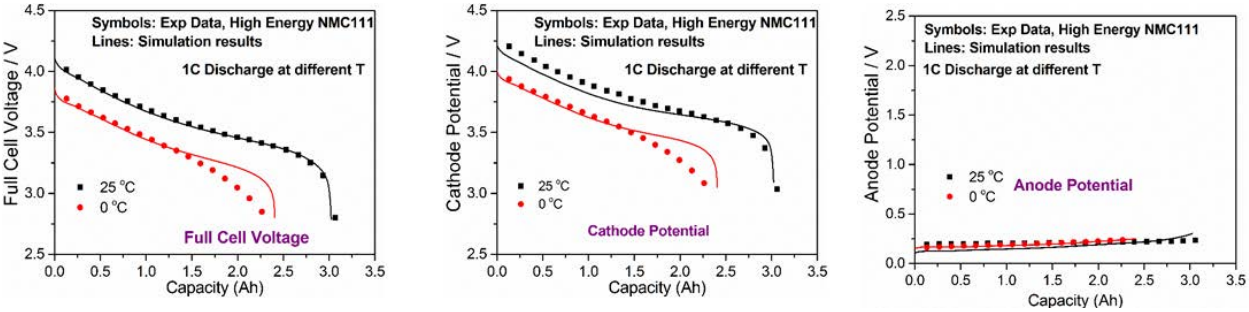

Figure 49. NMC111/C BOL performance: Model validation at different temperatures for high energy cell

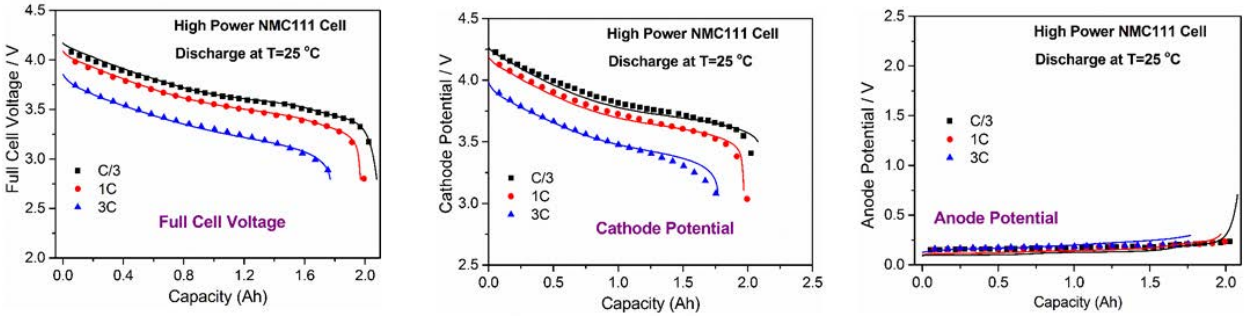

Figure 50. NMC111/C BOL performance: Model validation at different discharge C-rates for high power cell

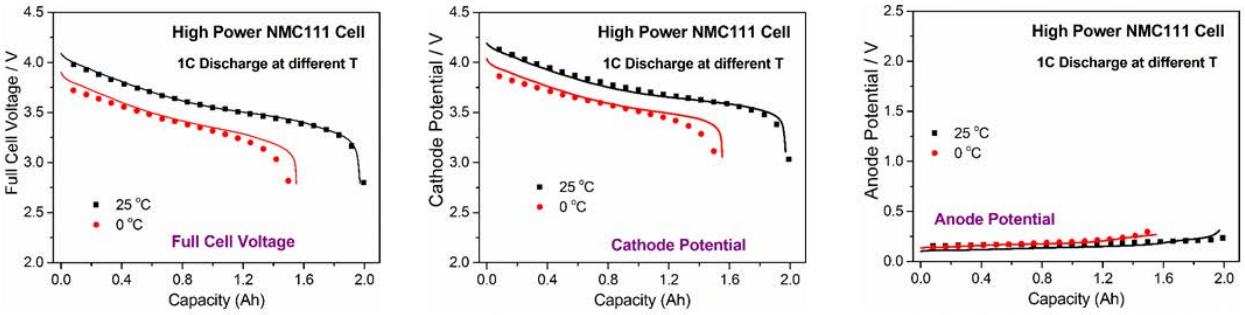

Figure 51. NMC111/C BOL performance: Model validation at different temperature for high power cell

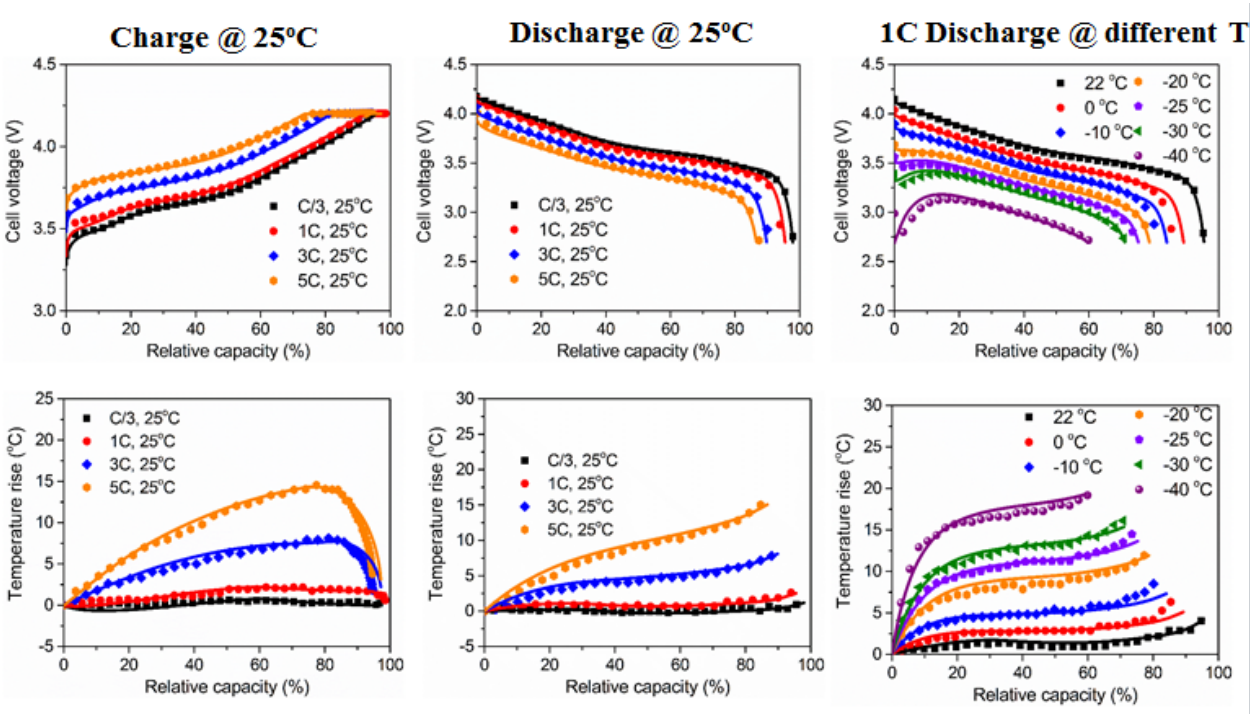

Figure 52. NMC622/C BOL performance: Model validation for high energy cell

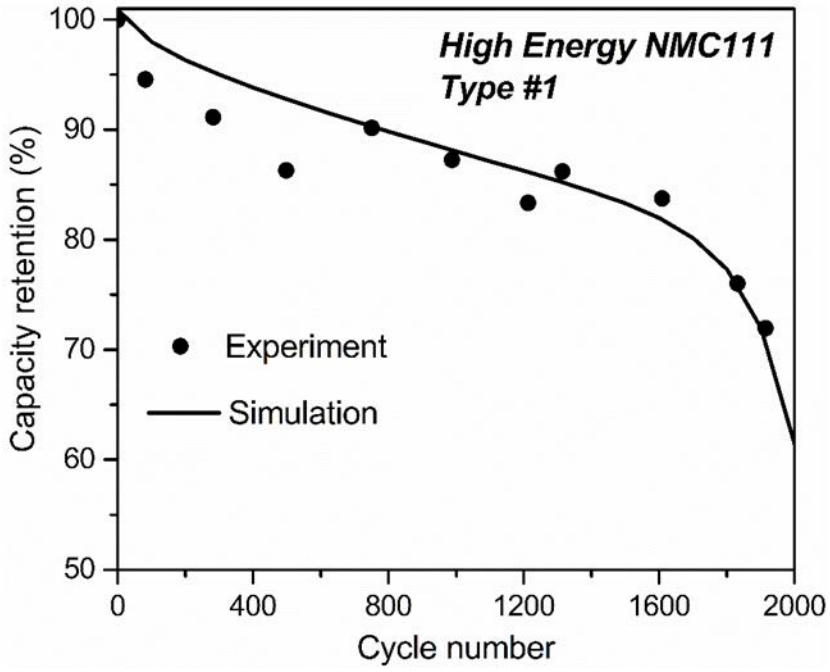

Figure 53. NMC111/C life model validation: C/3 capacity retention for high energy cell

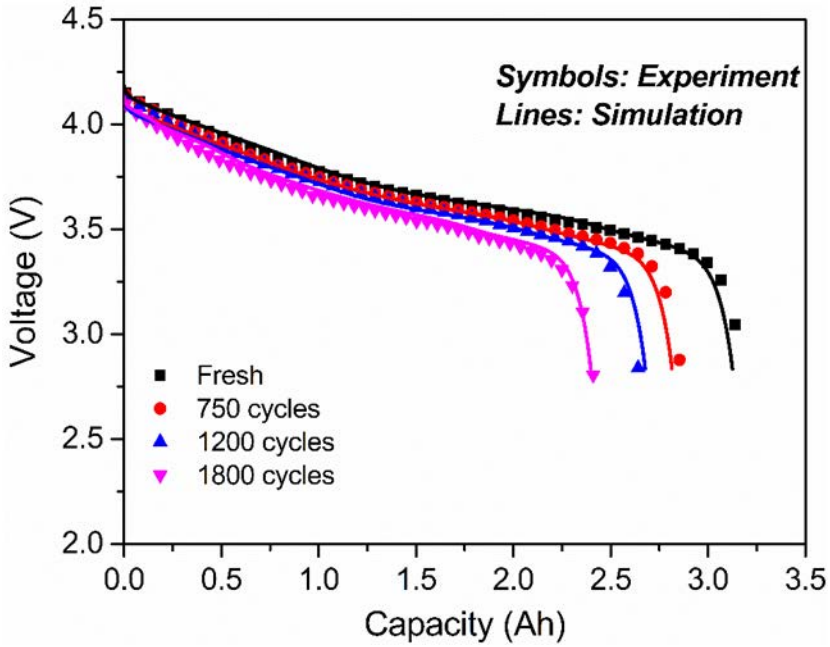

Figure 54. NMC111/C life model validation: C/3 discharge curves after various cycles for high energy cell

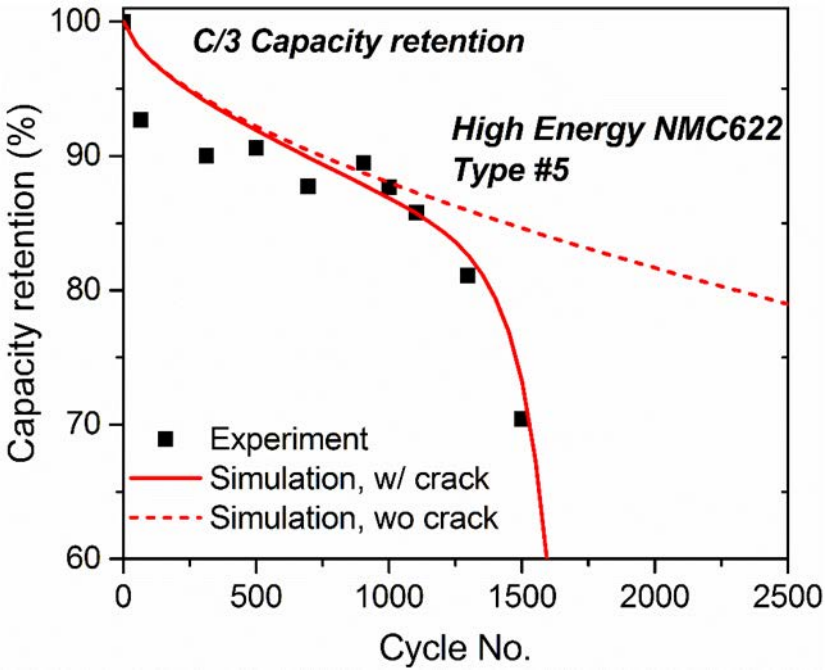

Figure 55. NMC622/C life model validation: C/3 discharge curves after various cycles for high energy cell

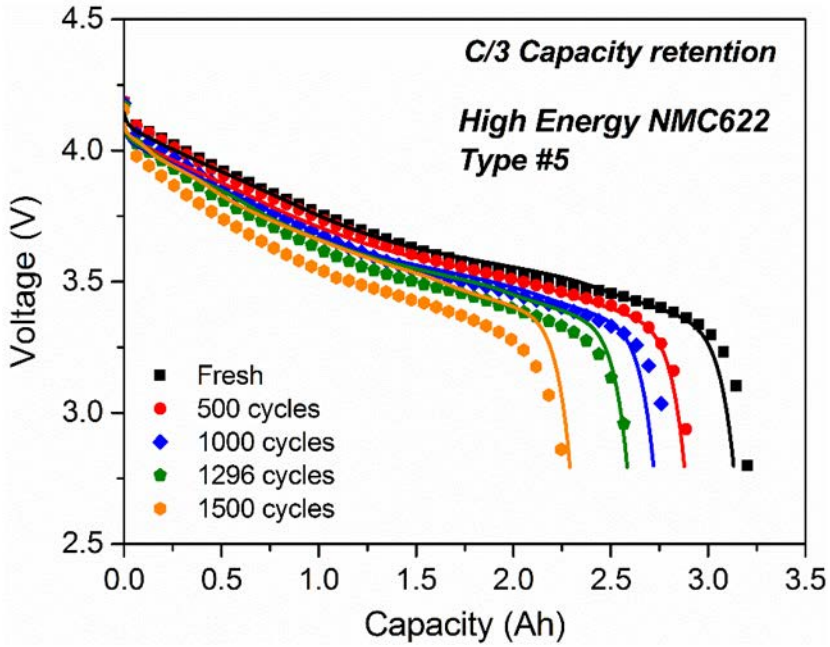

Figure 56. NMC6222/C life model validation: C/3 discharge curves after various cycles for high energy cell

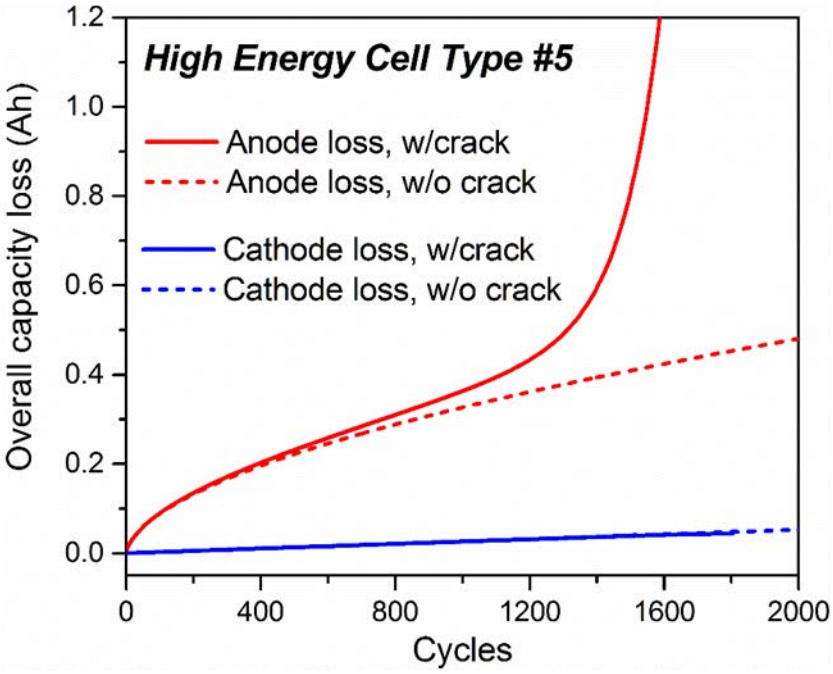

Figure 57. NMC6222/C life model analysis: capacity loss in anode and cathode with/without crack propagation for high energy cell

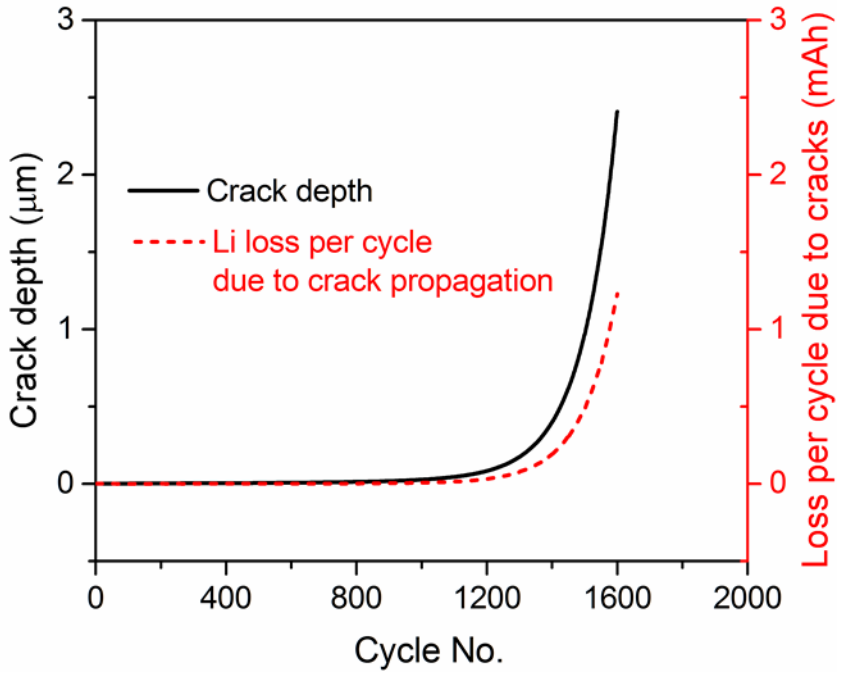

Figure 58. NMC6222/C life model analysis: crack depth and lithium loss due to crack propagation for high energy cell

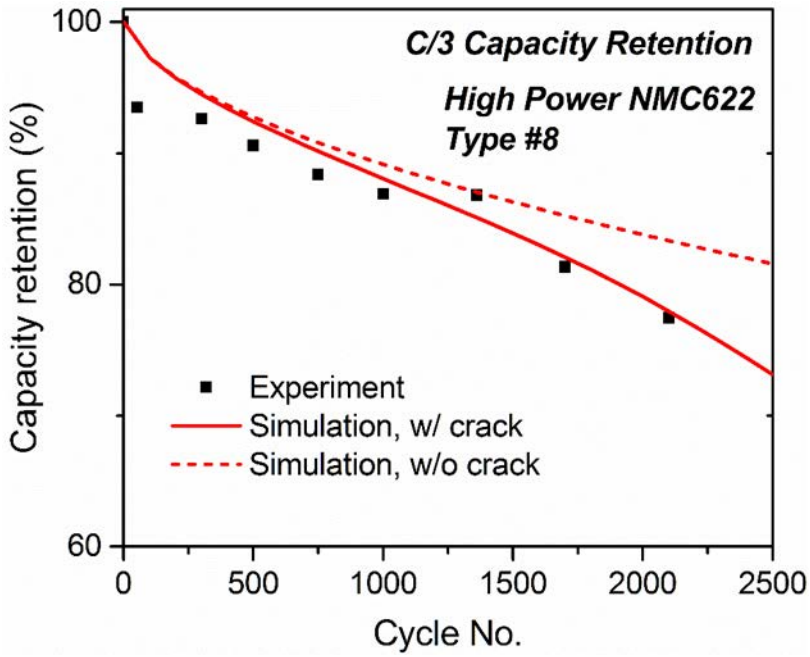

Figure 59. NMC622/C life model validation: C/3 discharge curves after various cycles for high power cell

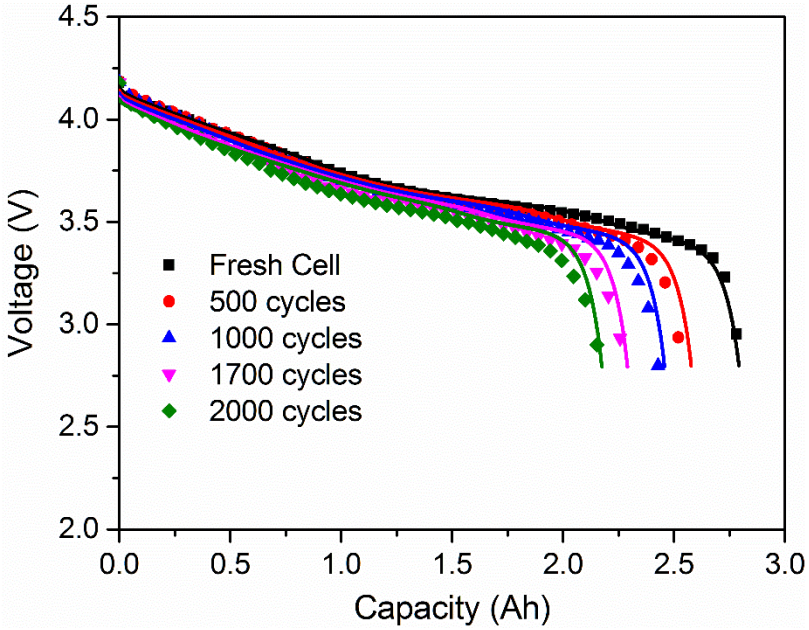

Figure 60. NMC6222/C life model validation: C/3 discharge curves after various cycles for high power cell

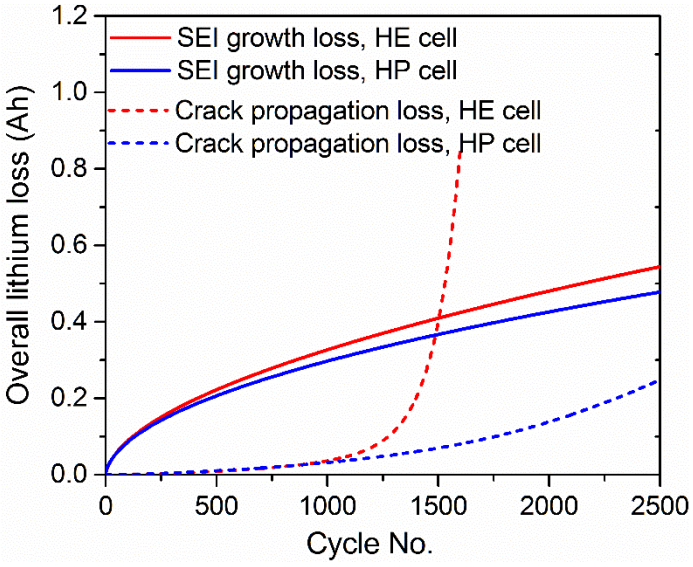

Figure 61. NMC6222/C life model analysis: capacity loss due to SEI growth and crack propagation for high energy and high power cells

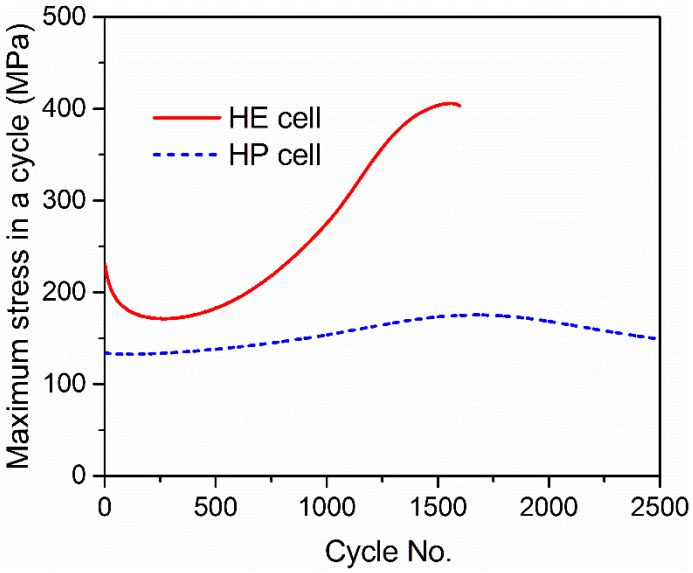

Figure 62. NMC6222/C life model analysis: maximum stress of each cycle for high energy and high power cells

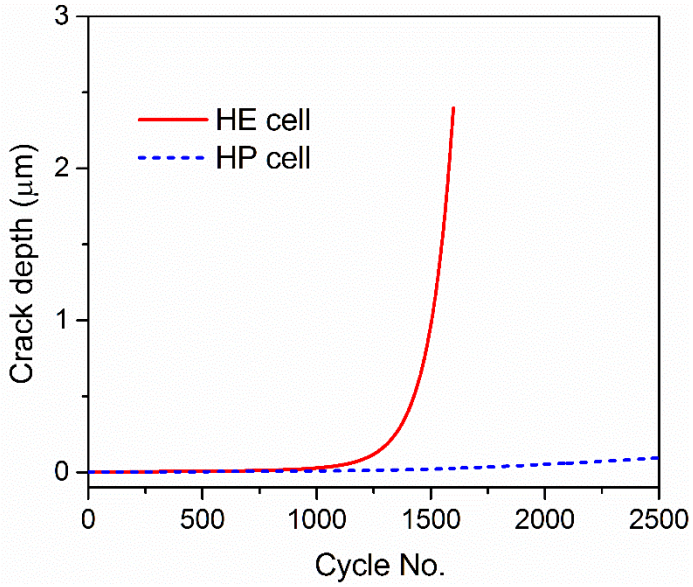

Figure 63. NMC6222/C life model analysis: crack depth due to crack propagation for high energy and high power cells

8. Coupling of ECT3D with Structural Mechanics Model via Open Architecture Standard (OAS)

In this task, we used the solidDisplacementFoam solver (OpenFoam 2.3) to do the linear stress analysis for the battery. Through this co-simulation, we have investigated thermal stress/strain field due to volume change of active materials, studied effects of constraint boundary condition to assess any difference between soft pouch and hardcase prismatic cells.

The results from this simulation are shown below. The rigid packaging causes 120 times more stress than soft packaging due to thermal expansion alone. Thus during the cell/pack design, reserving extra room for battery volume expansion is significantly important. As the cell manufacturer try to pack more energy into the cell/pack, the reserved room becomes smaller and smaller. If there is no enough space to accommodate cell expansion, the increase pressure within the cell might develop to separator puncture, leading to thermal runaway.

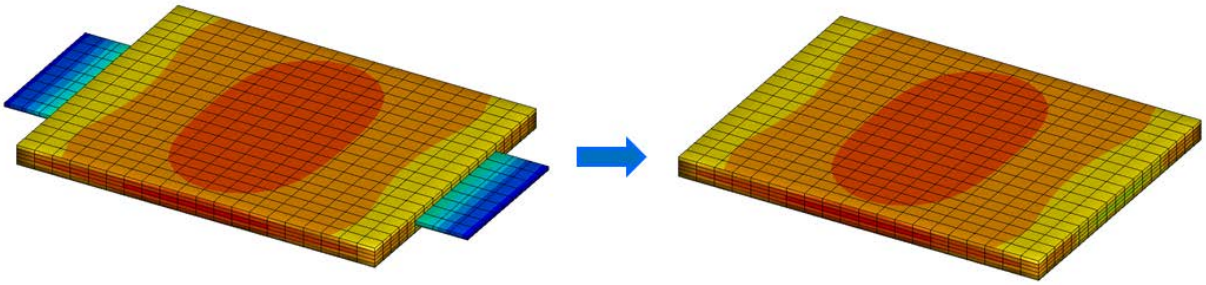

Ansys Fluent mesh (ECP software) **OpenFoam mesh created thru blockMesh**

Figure 64. Mesh for EC Power software and solidDisplacementFoam solver

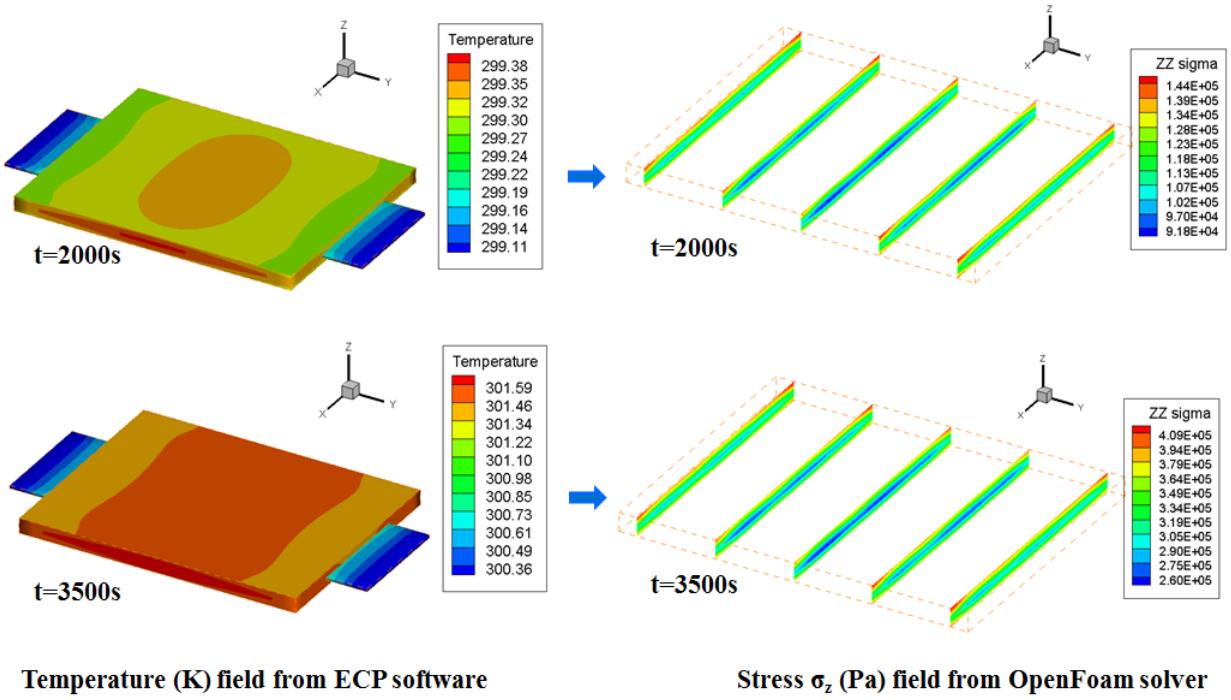

Figure 65. Simulation results for 1C discharge at two time instants, t=2000s and 3500s.

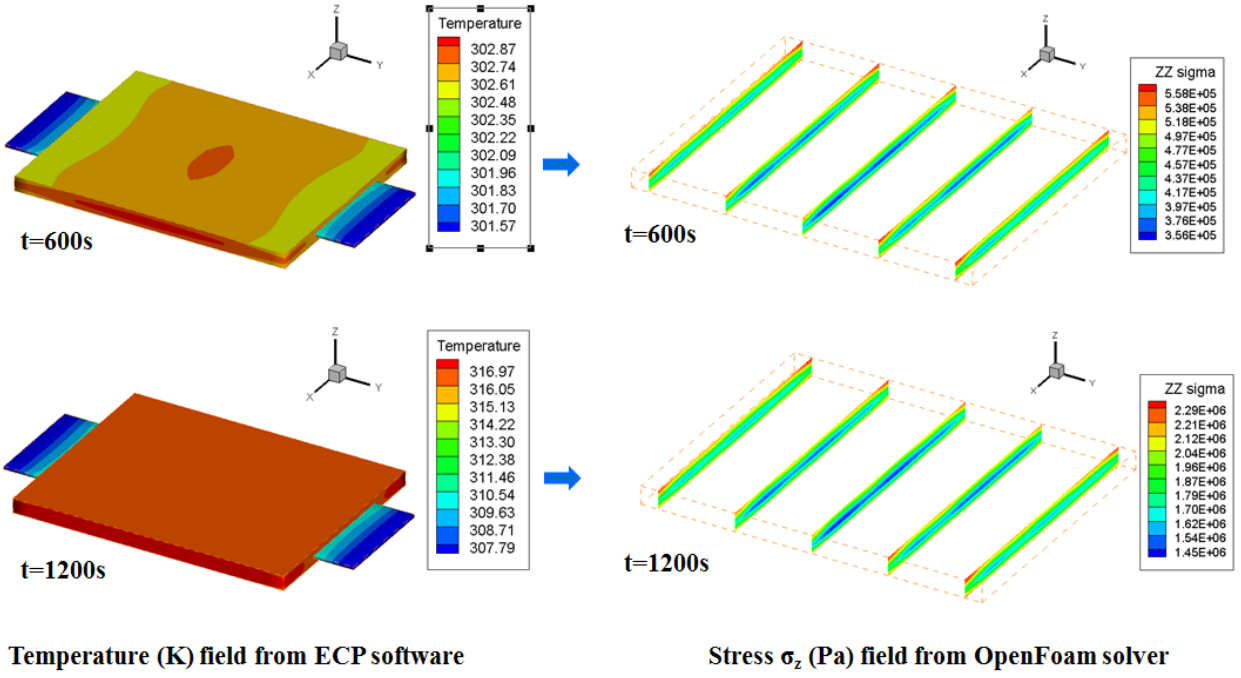

Figure 66. Simulation results for 3C discharge at two time instants, t=600s and 1200s

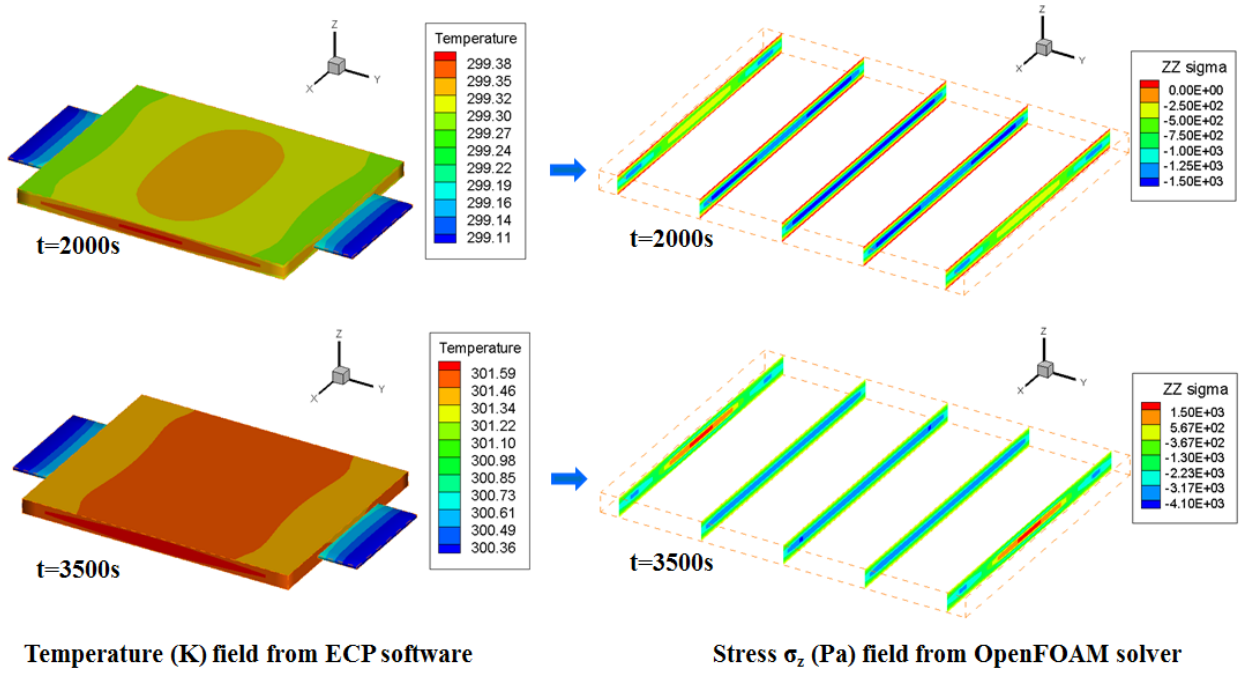

Figure 67. Simulation results for 1C discharge at two time instants, t=2000s and 3500s for soft packaging

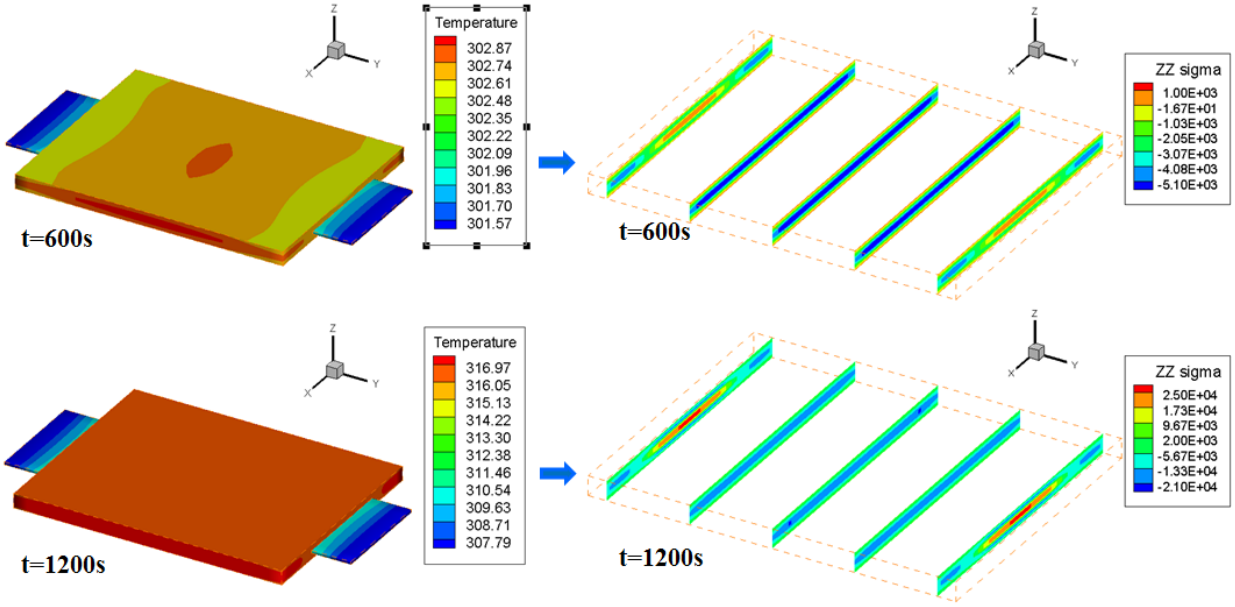

Temperature (K) field from ECP software **Stress σ_z (Pa) field from OpenFOAM solver**

Figure 68. Simulation results for 3C discharge at two time instants, t=600s and 1200s for soft packaging

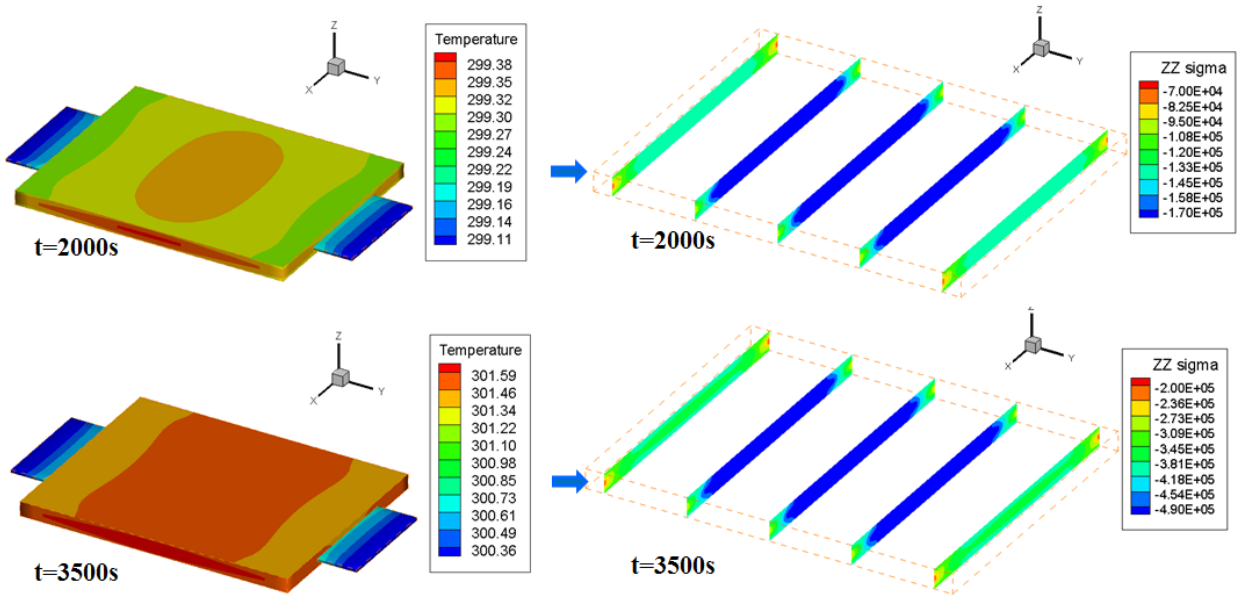

Temperature (K) field from ECP software **Stress σ_z (Pa) field from OpenFOAM solver**

Figure 69. Simulation results for 1C discharge at two time instants, t=2000s and 3500s for rigid packaging

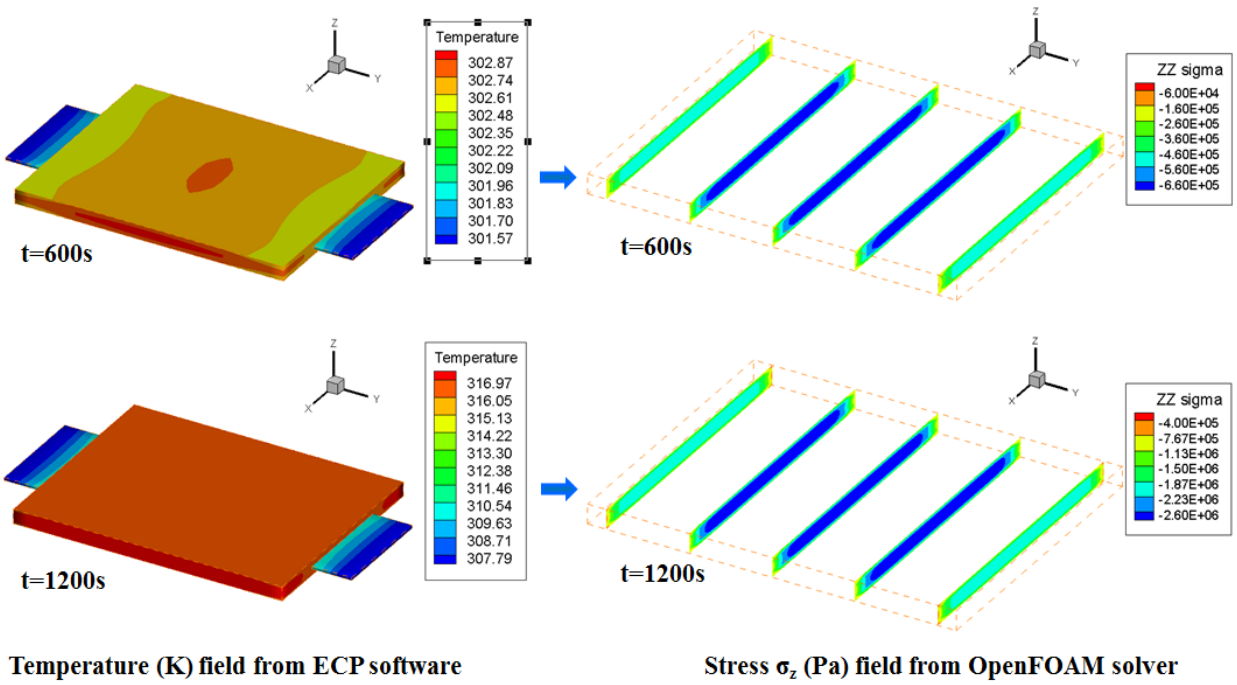

Figure 70. Simulation results for 3C discharge at two time instants, t=600s and 1200s for rigid packaging

9. Additional accomplishments from project

In addition to the successful completion of the primary goals and tasks of this project, we were able to successfully apply previously validated safety model towards the project goal. First we study the soft and hard shorting during charging. Then we apply the battery safety model to discover a safer battery structure for large EV cells.

Additionally, numerous papers and presentations were made through this project, and we have listed those below in order to emphasize the impact of this project work.

Soft vs hard internal shorting during charging

The recent Samsung Note battery incidents indicate that soft internal shorting could become a huge hazard in presence of battery charging (connected to a wall socket). Similar problems could occur in electric vehicles (garage charging overnight). We use the validated safety model to elucidate this problem and identify the map of safety. Here we simulate the internal shorting under the condition of CCCV charging process. It is shown that two different scenarios might occur depending on the magnitude of the shorting resistance (i.e. soft shorting or hard shorting).

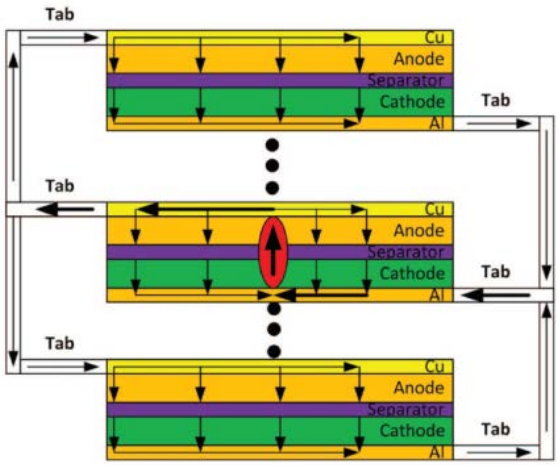

Figure 71 Current flow path in the internal shorting process

Figure 71 illustrates the current flow path in the internal short-circuit process, where a short-circuit object (SCO) is embedded within one electrode layer of the cell. The SCO creates a short circuit and current loop within the electrode layer where the SCO is located. This electrode layer not only discharges its energy to itself, it also serves as a load to the other electrode layers

without a SCO inside. The cases of internal shorting without charging follow the current flow pattern depicted in Figure 71.

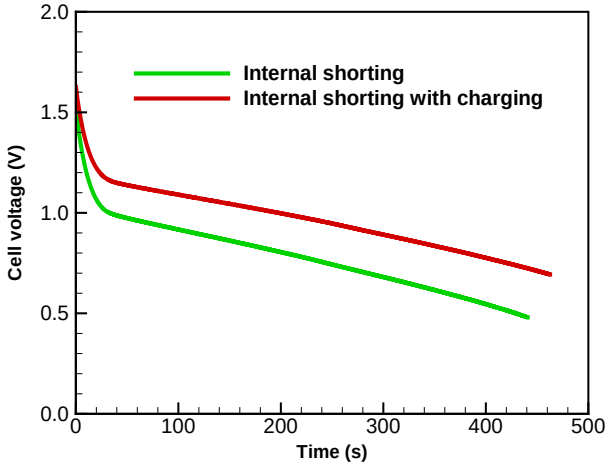

Figure 72 Voltage responses (10 mΩ)

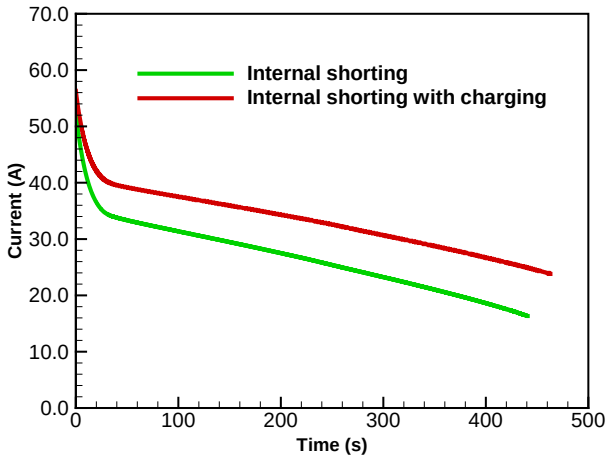

Figure 73 Current responses (10 mΩ)

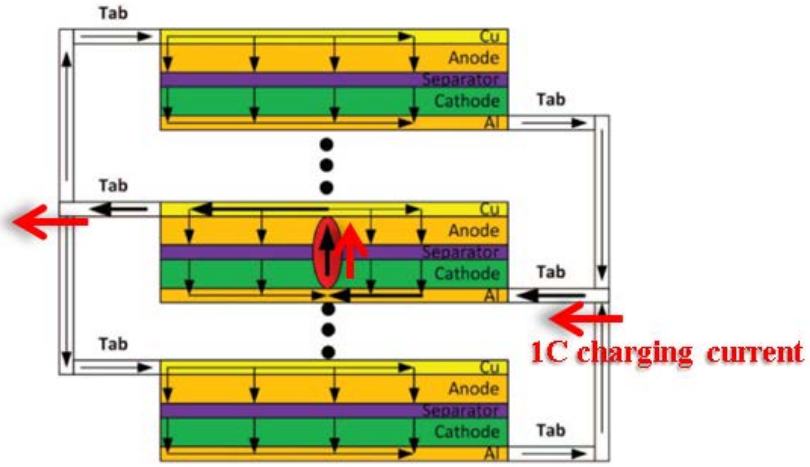

Figure 74 Current flow path in the internal shorting process with charging for small shorting resistance (10 mΩ)

Figure 72 shows the voltage evolution for 10 mΩ cases. It can be seen that the cell voltage is very low for the internal shorting only case. The charging voltage for the charging case is only slightly higher (around 170mV). This higher voltage is required in order to keep the 1C charging current. Figure 73 shows the current responses for 10 mΩ cases. The current is defined as the total current flow through the SCO in all of the figures in this study unless noted. The difference between the two current responses is very close to the 1C charging current (8A). The reason can be easily explained in Figure 74, which shows the current flow path for the internal shorting process with constant current charging for small shorting resistance (10 mΩ). Due to small charging voltage, all of the cell layers are in the discharging mode. The current flow path is the same as the internal short only cases as shown in Figure 71. The charging current is superimposed on the internal-short process. The 1C charging current only flows through the SCO. Figure 75 shows the temperature evolutions for 10 mΩ cases. Due to the additional charging current, the

temperature at the shorted location for the charging case is 70K higher than that of the internal shorting only case.

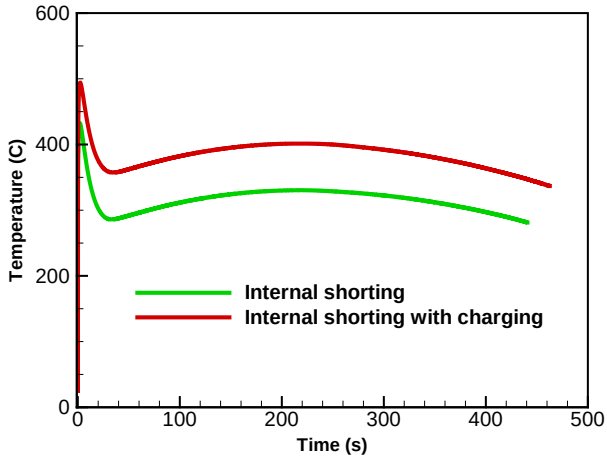

Figure 75 Temperature responses at shorted location (10 mΩ)

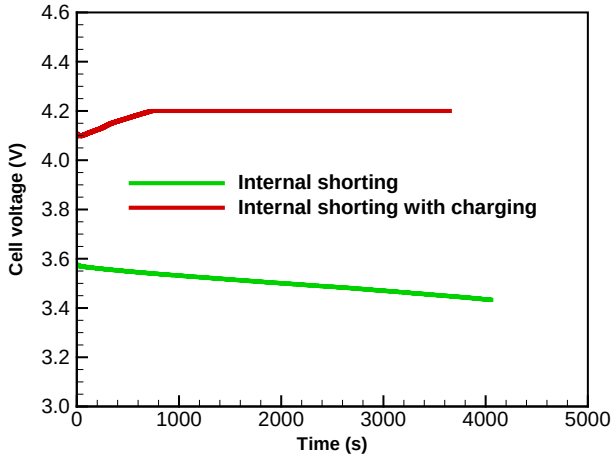

Figure 76 Voltage responses (2 Ω)

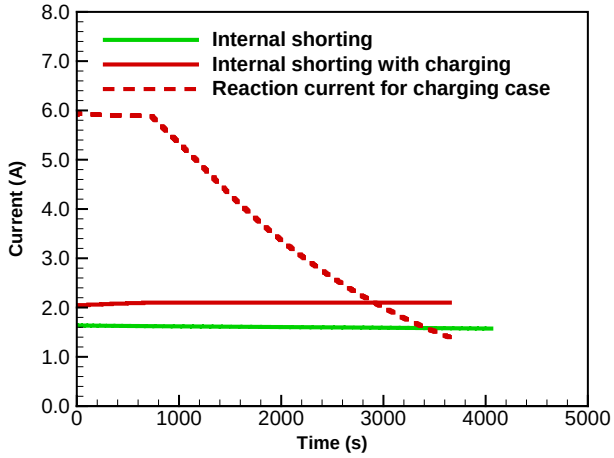

Figure 77 Current responses (2 Ω)

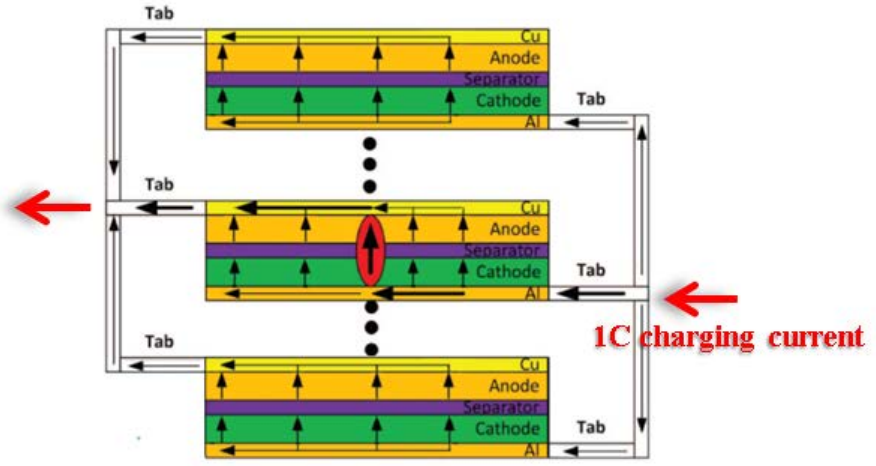

Figure 78 Current flow path in the internal shorting process with charging for large shorting resistance (2 Ω)

Figure 76 shows the voltage evolution for 2Ω cases (when there is a loose contact during soft shorting). For the internal shorting only case, the cell voltage shows a typical discharge curve when the load resistance is relatively large. However, the cell voltage for the charging case shows

a typical voltage response under CCCV charging process: the cell voltage increases with time initially, and then remains at a constant value (4.2V). Even during the internal shorting process, the cell still can be charged. Figure 77 shows the current responses for 2Ω cases. The current flow through the SCO is about 1.6A for the internal shorting only case. The SCO current (around 2.1A) can be roughly estimated using the charging voltage and shorting resistance for the charging case. Figure 78 shows a clear picture of the current flow path for the charging case with a large shorting resistance (2 Ohm). Like a normal cell charging process, the current flow pattern is totally different from patterns shown in Figures 71 and 74. Only part of the total charging current (around 2.1A) flows through the SCO. The rest of the charging current flows through the cell layers as the reaction current, as shown in Figure 77. Figure 79 shows the temperature evolutions for 2Ω cases. Since the SCO current of the charging case is much larger than that of the case without charging, the temperature at the shorted location for the charging case is much higher than that of the internal shorting only case. It can be seen that the maximum temperature in the case absent of charging is around 125^{o}C, perhaps still within the limit of battery safety without causing deformation of the separator and decomposition of the electrolyte. On the other hand, in the presence of charging, the maximum temperature rises above 170^{o}C, exceeding the limit of battery safety. Here lies a major difference in the consequence of soft shorting with and without charging current. Safety simulation appears to have explained the dramatic effect of charging current on a soft-shorting scenario of a Li-ion cell.

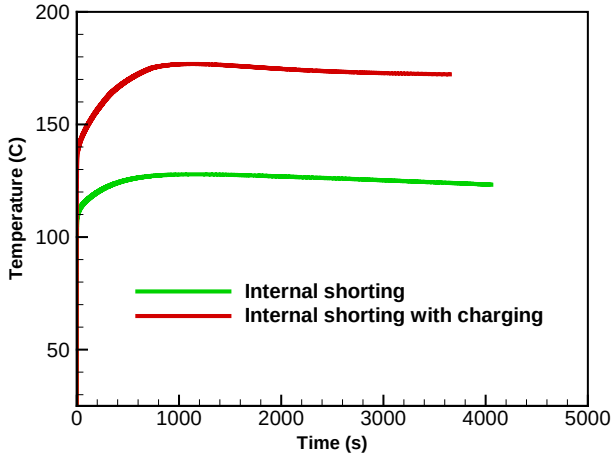

Figure 79 Temperature responses (2 Ω)

Safer cell structure for large EV cells

A larger cell capacity leads to more dangerous conditions upon internal short, simply by having greater energy to be dissipated during the short. In our safer cell design concept, we divide the one single cell into multiple zones by coating the positive temperature coefficient (PTC) material on the tabs, as shown in Figure 80. This zone defense mechanism will turn off the energy release from the neighboring zones when internal short occurs.

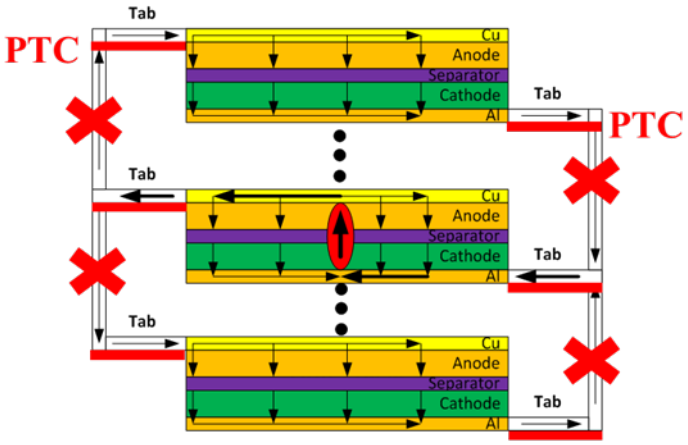

Figure 80 Turning off energy release by coating PTC on tabs

In order to validate the new design, we apply our battery safety model to a 32Ah NCM/C cell. The cell has dimensions of 150mm×100mm×11mm. Figure 81 show the mesh used for this simulation. As shown in Figures 82 83 84, the new design concept can successfully reduce the cell temperature to the safe level with a few seconds. We think we have potential to file a powerful patent for an inherently safe structure for EV batteries (94Ah in 2017 i3 or even 150 Ah in the future).

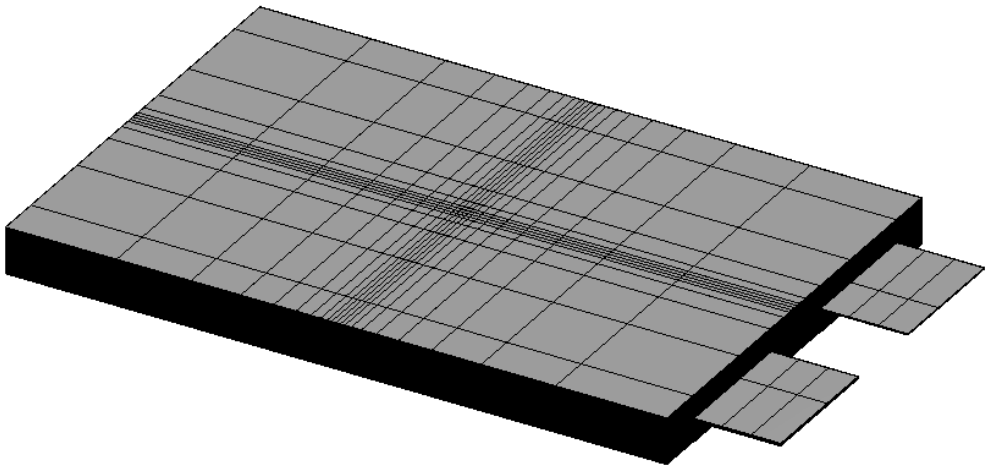

Figure 81 Mesh used for simulation

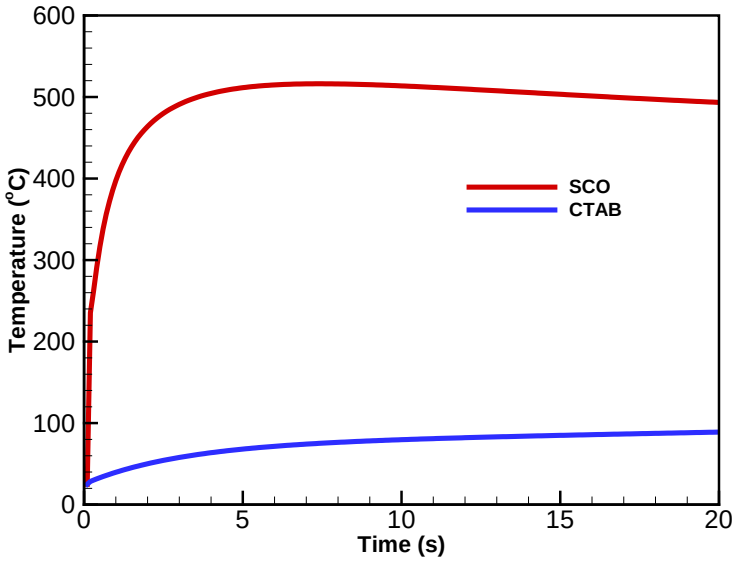

Figure 82 Temperature evolution for normal cell

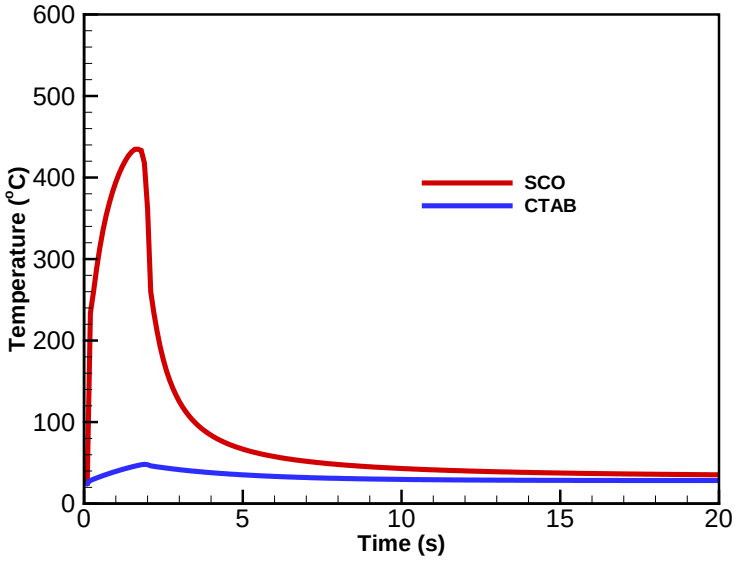

Figure 83 Temperature evolution for improved cell

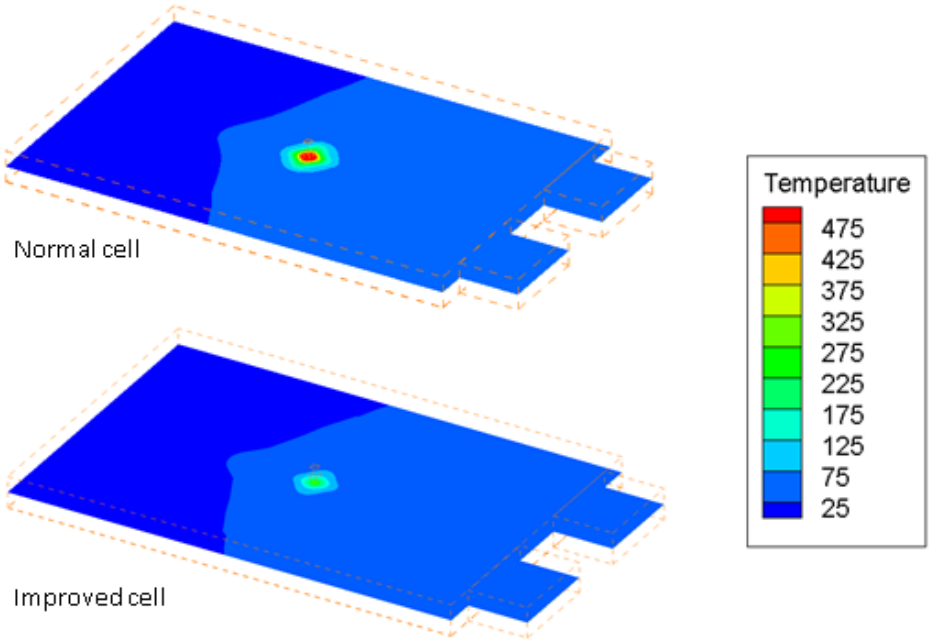

Figure 84 Temperature contour of the shorted plate at time=2s for normal and improved cells

Publications list

The following is a selected list of journal publications and presentations stemming from the work of the CAEBAT2 project:

Wei Zhao, Gang Luo, and Chao-Yang Wang, “Modeling Nail Penetration Process in Large-Format Li-Ion Cells”, Journal of The Electrochemical Society, 162 (1) A207-A217 (2015)

Wei Zhao, Gang Luo, and Chao-Yang Wang, “Modeling Internal Shorting Process in Large-Format Li-Ion Cells”, Journal of The Electrochemical Society, 162 (7) A1352-A1364 (2015)

GuangshengZhang, LeiCao, ShanhaiGe, Chao-YangWang, Christian E. Shaffer, and Christopher D. Rahn, “Reaction temperature sensing (RTS)-based control for Li-ion battery safety”, Scientific Reports, Vol. 5, pp. 18237-18242, 2015.

Wang, Q., Shaffer, C.E. and Sinha, P.K. (2015). "Controlling factors of cell design on large-format Li-ion battery safety during nail penetration," Front. Energy Res., 3:35.

Sinha, P., "Decoding Battery Explosions: New Opportunities for Safe Li-ion Battery Development," Battery Safety Conference 2015, Baltimore, MD, November 17-19, 2015.

Kalupson, J., Sinha, P., Shaffer, C. and Wang, C.Y., "Effects of Li-Ion Battery Pack Thermal Management on Performance and Life," 225th ECS Meeting, Abstract# 145, Orlando, FL, USA, May 11-15, 2014.

Kalupson, J., Wang, Q., Zhao, W., Sinha, P., Shaffer, C. and Wang, C.Y., "Cell- and Pack-Level Simulation of Large-Format Li-Ion Battery Safety Events," 225th ECS Meeting, Abstract# 160, Orlando, FL, USA, May 11-15, 2014.

X-G. Yang, C. Bauer, and C.Y. Wang, "Sinusoidal Current and Stress Evolutions in Lithium-ion Batteries," Journal of Power Sources, Vol. 327, pp. 414-422, 2016.

Chao-Yang Wang, G. Zhang, XG Yang, Dan Marple, YJ Leng, “Novel Battery Structures for Better Performance, Cycle Life & Safety,” US-China EV Battery Workshop, Denver, CO; April 26, 2016.

G. Zhang, S. Ge, T. Xu, X-G. Yang, H. Tian and C.Y. Wang, "Rapid Self-heating and Internal Temperature Sensing of Lithium-ion Batteries at Low Temperatures," Electrochimica Acta, Vol. 218, pp. 149-155, 2016.

C.Y. Wang, “Dramatically Improved Battery Safety with In-Cell Sensors and Actuators,” invited talk at Intl Battery Seminar, Fort Lauderdale, FL, March 21-24, 2017.

Y. Leng, S. Ge, D. Marple, X.G. Yang, C. Bauer, P. Lamp, and C.Y. Wang, "Electrochemical Cycle-Life Characterization of High Energy Lithium-ion Cells with Thick Li(Ni0.6Mn0.2Co0.2)O2 and Graphite Electrodes," Journal of the Electrochemical Society, Vol. 164, pp. A1037-1049, 2017.

X.G. Yang, Y. Leng, G. Zhang, S. Ge and C.Y. Wang, Modeling of lithium plating induced aging of lithium-ion batteries: Transition from linear to nonlinear aging,” Journal of Power Sources, 360, pp. 28-40, 2017.

C.Y. Wang, “Smart batteries enabled by in-cell sensors and actuators,” invited talk at Beyond Li-ion X, San Jose, CA, June 27-29, 2017.

10. Conclusions

Over the past 3+ years the EC Power-led CAEBAT2 team has worked to fulfill the goals laid out at the beginning of the project. The team has met and in some cases exceeded these goals. We have accomplished the following major milestones:

- Expanded extensive materials database by characterizing and adding NCM622 and NCA cathode materials and Si/C anode material.
- Completed cell and pack nail penetration tests.
- Completed development of a nail penetration model and finished cell and pack model validation.
- Completed cycle life tests of NCM111 and NCM622 cells for both high power and high energy types.
- Developed a comprehensive cycle life model by incorporating the new crack formation-growth mechanism and completed model validation against four cells with both high power and high energy types and two cathode materials, NCM111 and NCM622.
- Completed overcharge tests for both NCM and NCA cells.
- Developed a new battery overcharge model and performed model validation against NCM and NCA cell data.
- Completed coupling of ECT3D with structural mechanics model via Open Architecture Standard (OAS).
- Investigated the soft and hard shorting during charging using validated safety model.
- Validated a safer battery structure for large EV cells using validated safety model.

We feel that most importantly, the project has been successful in two aspects:

- The project and project funding has led to a more refined ***commercial Li-ion battery design software*** that cuts cost and time from the design phase of automotive Li-ion batteries and packs. It will continue to make an impact in the battery and automotive community, well beyond the close of this project. Our ***commercial Li-ion battery design software*** with above-mentioned expanded capabilities is being used by defense and aerospace industries.

- The team has been active in ***publishing, presenting, and sharing the results*** from the project to the battery and automotive community at large, thereby making an impact on the ***progression of automotive large-format Li-ion battery technology***.

As these successes, in addition to the other successful activities and outcomes of the project, are in line with the overarching goals of the CAEBAT2 program, we feel that this project can be deemed a success.

References

[1] M. Anderson, “Energy System for Large Displacement Unmanned Undersea Vehicle Innovative Naval Prototype (INP),” US Office of Naval Research Presentation, http://auvac.org/publications/view/158 (2011).

[2] Y. Ji, Y. Zhang, and C.Y. Wang, J. Electrochem. Soc., 160, A639 (2013).

[3] C.E. Shaffer, C.Y Wang, G. Luo, and W. Zhao, “Safety Analysis Design of Lithium-ion Battery EV Pack through Computer Simulation” Battery Safety 2012, Knowledge Foundation Conference, December 6-7, 2012, Las Vegas, NV

[4] M. Doyle, T.F. Fuller, and J. Newman, J. Electrochem. Soc. 140, 1526 (1993).

[5] W.B. Gu and C. Y. Wang, “Thermal and electrochemical coupled modeling of a lithium ion cell”, in Lithium Batteries, ECS Proceedings, 99-25, 748 (2000).

[6] V. Srinivasan and C. Y. Wang, J. Electrochem. Soc., 150, A98 (2003).

[7] K. Smith and C. Y. Wang, J. Power Sources, 160, 662 (2006).

[8] Joan Lowy, The Boston Globe, “FAA set to lift grounding order on 787s”, April 20, 2013.

[9] Yancheng Zhang, Chao-Yang Wang, Xidong Tang, Journal of Power Sources, 196 1513, 2011.

[10] W. Fang, O.J. Kwon, and C.Y. Wang, Int. J. Energy Res., 34, 107 (2010).

[11] Y.T. Cheng, M.W. Verbrugge, J. Power Sources 190 (2009) 453e460.